The Global Monsoon as Seen through the Divergent Atmospheric Circulation

KEVIN E. TRENBERTH, DAVID P. STEPANIAK, AND JULIE M. CARON

National Center for Atmospheric Research, Boulder, Colorado*

(Manuscript received 23 July 1999, in final form 27 October 1999)

ABSTRACT

A comprehensive description is given of the global monsoon as seen through the large-scale overturning in the atmosphere that changes with the seasons, and it provides a basis for delimiting the monsoon regions of the world. The analysis focuses on the mean annual cycle of the divergent winds and associated vertical motions, as given by the monthly mean fields for 1979–93 reanalyses from the National Centers for Environmental Prediction–National Center for Atmospheric Research (NCEP–NCAR) and European Centre for Medium-Range Weather Forecasts (ECMWF), which are able to reproduce the dominant modes. A complex empirical orthogonal function analysis of the divergent circulation brings out two dominant modes with essentially the same vertical structures in all months of the year. The first mode, which depicts the global monsoon, has a simple vertical structure with a maximum in vertical motion at about 400 mb, divergence in the upper troposphere that is strongest at 150 mb and decays to zero amplitude above 70 mb, and convergence in the lower troposphere with a maximum at 925 mb (ECMWF) or 850 mb (NCEP). However, this mode has a rich three-dimensional spatial structure that evolves with the seasons. It accounts for 60% of the annual cycle variance of the divergent mass circulation and dominates the Hadley circulation as well as three overturning transverse cells. These include the Pacific Walker circulation; an Americas–Atlantic Walker circulation, both of which comprise rising motion in the west and sinking in the east; and a transverse cell over Asia, the Middle East, North Africa, and the Indian Ocean that has rising motion in the east and sinking toward the west. These exist year-round but migrate and evolve considerably with the seasons and have about a third to half of the mass flux of the peak Hadley cell. The annual cycle of the two Hadley cells reveals peak strength in early February and early August in both reanalyses.

A second monsoon mode, which accounts for 20% of the variance, features relatively shallow but vigorous overturning with the maximum vertical velocities near 800 mb, outflow from 750 to 350 mb, and inflow peaking at 925 mb. It is especially strong over Africa where the shallow, mostly meridional overturning migrates back and forth across the equator with the seasons. It influences the Middle East, has a signature over Australia, and is also an important component of the overturning in the tropical eastern Pacific and Atlantic, and thus of the convergence zones in these regions.

The relationship of the global monsoon to the regional monsoons is described over six zonal sectors: Africa, Australia–Asia, North America, South America, and the Pacific and Atlantic Oceans. Only the two ocean areas do not undergo a seasonal reversal required for monsoons, although they have direct overturning cells and they nevertheless participate in the global monsoon through the changes in large-scale overturning. The regional meridional cross sections highlight the importance of the shallow overturning cell in lower-troposphere monsoon activity. The steadiness of the overturning circulation is determined by comparing the signal of the seasonal mean vertical motions at 500 mb with the standard deviation of the transient daily variations. Locations where this signal exceeds 60% of the daily noise correspond closely with the regional centers of the monsoon.

1. Introduction

The term ''monsoon'' stems from seasonal variations in winds but it is now more generally applied to tropical and subtropical seasonal reversals in both the atmospheric circulation and associated precipitation. These changes arise from reversals in temperature gradients between continental regions and the adjacent oceans with the progression of the seasons, and the extremes are often best characterized as ''wet'' and ''dry'' seasons rather than summer and winter. Moreover, in spite of the absence of seasonal migration of the Pacific and Atlantic intertropical convergence zones (ITCZs) between the hemispheres, it is evident that there is a global-scale monsoon, by which we mean a global-scale persistent overturning of the atmosphere throughout the Tropics and subtropics that varies with time of year. The reason why the global aspect should also be emphasized is because of the coordination brought about by the annual cycle of the solar heating and their apparent con-

* The National Center for Atmospheric Research is sponsored by the National Science Foundation.

Corresponding author address: Dr. Kevin Trenberth, NCAR/CGD, P.O. Box 3000, Boulder, CO 80307-3000.
E-mail: trenbert@ucar.edu

nections in the global divergent circulation necessitated by mass conservation. Embedded within this global monsoon are the more conventional regional monsoons. The dominant monsoon systems in the world are the Asian–Australian, the African, and the American monsoons, although the latter has not been clearly identified with the wind reversals (Webster et al. 1998). In these sectors of the Tropics, the wet season migrates from one hemisphere to the other following the sun, and the large-scale overturning atmospheric circulation reverses.

The picture of a monsoon overturning circulation, as something like a thermally driven sea breeze on a larger scale, and therefore modified somewhat by the earth's rotation is, however, highly idealized. Moreover, often only the cross-equatorial overturning comprising the local Hadley circulation has been emphasized: it is referred to as the ''lateral monsoon'' in Webster et al. (1998). Strong rising motions in the summer hemisphere at perhaps 10° latitude locally are to some extent compensated by subsidence at 20° latitude in the winter hemisphere.

However, in the Tropics, a large component of the overturning is not meridional but is instead zonally oriented. Although originally defined by Bjerknes (1969) to refer to the circulation in the Pacific near the equator, the term ''Walker circulation'' is often used to refer to this broader east–west overturning. Krishnamurti (1971) and Krishnamurti et al. (1973a) emphasized that the Walker circulation was but part of a broader east–west circulation. Those studies for the first time hinted at the essence of the full overturning in the atmosphere. Webster et al. (1998) use the term Walker circulation in the Pacific but ''transverse monsoon'' for overturning toward the west. Some parts of the Tropics, including the tropical Atlantic and central and eastern Pacific Oceans ITCZs, which reside between about 5 and 10°N year-round, do not appear to change much with season. However, it does not necessarily imply that the downward branch is similarly anchored and it is desirable to explore whether the connectivity varies with time of year.

The three-dimensional character of the atmospheric circulation is dominated by the rotational (nondivergent) component but influenced by the divergent circulation. Large momentum transports occur in the meridional circulation and strongly influence the subtropical jet streams, so that the strongest jet of over 70 m s^{-1} lies off the east coast of Asia in the boreal winter and, in the austral winter, the strongest jet of over 50 m s^{-1} lies off the east coast of Australia. Both are directly associated with the regions of the globe where and when the strongest overturning occurs in lower latitudes.

The existence of the direct overturning circulation implies that heat is being transported to cooler regions. Sources of energy come from sources of heating in the atmosphere and, in a large sense, there has to be a transport by the atmosphere and ocean from source to sink. Heating occurs in the Tropics, where it is already hot, and cooling occurs at higher latitudes. Moist static energy is gained in the Tropics and lost at higher latitudes; see Webster (1994) for an overview. A small amount is converted to kinetic energy and regained as friction heating. Overall, air parcels moving poleward must have a higher moist static energy than air parcels moving equatorward. In midlatitudes the poleward heat transport is carried out by transient baroclinic eddies and stationary waves, while in the Tropics the transport is dominated by large-scale overturning (Trenberth and Solomon 1994). Thus the Hadley and Walker cells are thermally driven cells that transport moist static energy. The dominant energy outflow center coincides closely with the region of highest sea surface temperatures in the oceans and this migrates back and forth across the equator following the sun. The vertically integrated heat and energy transport in two dimensions carried out by the divergent circulation will be dealt with in a companion paper.

The main purpose of this paper is to document the global monsoon as seen through the mean annual cycle of the large-scale overturning in the divergent atmospheric circulation and, in particular, to examine its three-dimensional spatial structure. We reexamine when the Hadley and Walker circulations are strongest, links to precipitation, and how the global monsoon varies by sectors (African, Australian–Asian, Pacific, North and South American, and Atlantic). We also indicate ways to graphically depict the mass flows.

A key issue is also the extent to which one should think of the global monsoon as a steady circulation (Ramage 1971), albeit made up of small-scale disturbances locally (see Fein and Stephens 1987). Thus there are active and break periods in regional monsoons and many identified subseasonal variations, as well as pronounced interannual variability (e.g., Webster et al. 1998). These aspects are pursued in section 6.

A comprehensive description of the divergent circulation of the atmosphere has been elusive owing to the difficulty of obtaining reliable fields. Errors in observations are often of the same order as the expected divergent component itself and huge observational gaps exist over the oceans. Analyses based on radiosonde observations contain major uncertainties (Trenberth and Solomon 1994), although of special note in this regard are the two volumes by Newell et al. (1972, 1974). Accordingly, the only viable approach is via four-dimensional data assimilation (4DDA) but past results have been model dependent. This aspect is discussed in section 2. However, for the first time, the mean annual cycle is reasonably reproducible in the reanalyses from the National Centers for Environmental Prediction–National Center for Atmospheric Research (NCEP–NCAR) and European Centre for Medium-Range Weather Forecasts (ECMWF), providing a new level of confidence in the results.

The data are described more fully in section 2. The main analysis of the three-dimensional distribution of the divergent winds is described in section 3 and it

brings out the two dominant modes of overturning that exist, one a deep mode throughout the tropical and subtropical troposphere, and the other a much shallower mode. The predominant east–west overturning circulations are examined in section 4 and the zonal mean meridional circulation is presented in section 5, along with the perspective from the mean vertical motion analysis at 500 mb. Section 6 examines the steadiness of the monsoon circulations and section 7 briefly provides a perspective on the regional monsoons. The results are discussed in section 8.

2. Data

The reanalyses from NCEP–NCAR (Kalnay et al. 1996) and ECMWF (Gibson et al. 1997) have been used to compute the detailed atmospheric mass budgets. The period used is that of the common data from 1979 to 1993. The global analyses are produced on model (sigma or hybrid) surfaces that consist, in simplest form, of a sigma (σ) terrain-following coordinate in which the lowest level corresponds to $p = p_s$, where p is pressure, p_s is the surface pressure, and $\sigma = p/p_s$. Hybrid η coordinates consist of σ near the surface but with a gradual transition to pressure with height. However, model coordinates have major disadvantages for computing time average diagnostics owing to the variability of the coordinate system with resolution, in time, and between centers, associated with the varying surface pressures (Trenberth 1995). Thus, in this paper, use is made of the four times daily pressure level data to enable us to explore the vertical structure and relationships of the divergent mass circulation as a function of pressure level.

The NCEP system is based on a numerical weather prediction model with T62 spectral resolution and 28 sigma levels in the vertical with five of those levels in the atmospheric boundary layer. The spectral statistical interpolation scheme is employed in the analysis with complex quality control. Fields are not initialized. An evaluation of some aspects of the NCEP–NCAR reanalyses from the standpoint of moisture transport is given by Mo and Higgins (1996), and they note that there is very little spinup between 0–6- and 12–24-h forecast values of the NCEP model evaporation, although there is some precipitation spinup of 0.1–0.2 mm day^{-1}, with maxima in the Tropics. Trenberth and Guillemot (1998) provide a comprehensive evaluation of the NCEP–NCAR reanalyses focused on the hydrological cycle. For convenience we refer to these as the NCEP reanalyses.

The ECMWF reanalyses are at T106 resolution and 31 levels in the vertical with a hybrid coordinate that transitions to a pressure coordinate above about 100 mb. Of note is that a diabatic, nonlinear normal mode initialization was applied. Evaluations of performance of the system are given by Uppala (1997) and Kållberg (1997), and by Stendel and Arpe (1997) for the hydrological cycle for both reanalyses.

In the pressure coordinate archive, the 17 levels available from the reanalyses are p = 1000, 925, 850, 700, 600, 500, 400, 300, 250, 200, 150, 100, 70, 50, 30, 20, and 10 mb from NCEP, while ECMWF includes a 775-mb level but does not have a 20-mb level. If the standard levels are denoted by $p_1, p_3, \ldots, p_{2J-1}$, where p_1 = 1000 mb and p_{33} = 10 mb for the 17 levels. Then we define the intermediate half levels as $p_j = \frac{1}{2}(p_{j-1} + p_{j+1})$, $j = 2, 4, 6, \ldots, 2J - 2$.

The analysis concentrates on the divergent atmospheric circulation in which the velocity **v** is split into rotational and divergent parts. The divergent atmospheric circulation has always been difficult to come to grips with because the divergent wind is poorly observed. The use of 4DDA to produce global analyses has resulted in estimates of the divergent circulation but this has not been fully physically constrained and results tend to be very model dependent. Accordingly, the strength of the divergent circulation has changed almost every time there is a change in the assimilating model physics (Trenberth and Olson 1988; Trenberth 1992). Therefore we use both the NCEP and ECMWF reanalyses to perform all analyses and check to see which features are robust. Physical constraints, especially those related to mass conservation, are exploited and all analyses are adjusted to ensure conservation of mass, as in Trenberth (1991a).

Agreement between the two analyses is not a guarantee that the result is correct. However, lack of agreement ensures that at least one analysis is incorrect. Many aspects of the divergent circulation in the two reanalyses in fact show surprising agreement in view of differences that were evident in the operational analyses (e.g., Trenberth and Olson 1988; Trenberth and Guillemot 1995). Moreover, the improvements in 4DDA over the years suggest that there is convergence toward the truth. However, Trenberth and Guillemot (1998) concluded that there was a negative bias in tropical precipitation in the NCEP reanalyses, which is probably an indication that the divergent circulation is too weak. Overall, ECMWF reanalysis precipitation fields are judged to be superior to those of other reanalyses when compared with Global Precipitation Climatology Project (Huffman et al. 1997) observational data by Stendel and Arpe (1997). Annamalai et al. (1999) also find the ECMWF reanalyses to be superior in describing the summer Asian monsoon. In spite of this, the strength of the Hadley circulations in the NCEP and ECMWF reanalyses are quite similar, as we shall show. But operational analyses from ECMWF indicate that Hadley circulation in the ECMWF reanalysis is weaker than more recent estimates, such as those in the system proposed for the ERA-40 reanalysis project (P. Kållberg 1999, personal communication).

To examine the divergent circulations regionally, it is necessary to use vectors to indicate the magnitude

and direction of the mass flows, as the circulations in a limited domain generally will not be closed. Accordingly, we carefully designed the graphics so that the arrows indicating the horizontal and vertical velocity vectors give the true direction of the mass flow with the length of the arrow appropriately scaled when plotted. Previously, such as in Webster (1994), the two components of the velocity were arbitrarily scaled to depict the overturning, instead of the true mass flux. The details are given in the appendix. Sometimes the plots are deceptive owing to the huge disparity in the horizontal and vertical scales of the axes. For closed circulations, where mass is conserved (such as for the meridional means in Fig. 4 and the zonal means in section 5), a mass stream function can be computed as a supplement and checked on the vectors, as also given in the appendix.

3. Three-dimensional structure of the divergent circulation

In this section we analyze the divergent atmospheric circulation to determine the vertical structure of the dominant modes for each month, season, and year, and the corresponding spatial structures.

a. Method

For each layer, each variable is mass weighted such that $\mathbf{v}_j$, for example, is replaced by $\mathbf{v}_j(p_{j-1} - p_{j+1})/g$, with appropriate weighting near the surface to take account of the surface pressure. We then analyze these variables to determine the vertical structures in the divergent wind field by taking complex empirical orthogonal functions (CEOFs). We consider a monthly mean field of mass weighted velocity, weighted by the square root of the cosine of latitude, to preserve the total area weighted variance. Because velocity is a vector, we treat the two components as a complex value. Then we form the complex covariance matrix of the different layers in the vertical as a vector and determine the eigenvalues of the resulting matrix, which determines how much variance is accounted for by the eigenvectors; see Trenberth and Shin (1984) for examples.

In atmospheric sciences it is common to have a field of variables and perform the eigenvector analysis on the temporal variations, so the elements in the covariance matrix correspond to the variances along the diagonal and the covariances off diagonal. The result is a spatial pattern as the eigenvector and a time series as the principle component. In our example, pressure level is used instead of time, and because we are analyzing a vector, the principle component is a complex vertical structure function, which has associated with it a complex spatial pattern. The latter simply represents the mass flow and is readily plotted as a vector. The former has an amplitude and a phase, so that for definiteness, if we choose the phase at the surface at 1000 mb to be in one direction, we can determine the direction of the vectors at every other level. Because mass is conserved, it is unlikely that propagation will occur in the vertical structure with the vectors pointing in several directions; instead we expect that the only viable modes will be ''standing'' modes in which the vectors all point in one direction or the opposite direction, and the vertical integral must be almost zero. Indeed this is the case except for transition zones where the amplitude is small and insignificant.

TABLE 1. For the various complex EOF analyses from the NCEP–NCAR reanalyses, the percentage variance accounted for by the first two EOFs. The seasons are Dec–Feb (DJF), Mar–May (MAM), Jun–Aug, and Sep–Nov.

Month	CEOF1	CEOF2
Jan	62.8	16.6
Feb	60.7	19.2
Mar	49.6	26.0
Apr	45.3	29.8
May	52.6	26.2
Jun	63.8	20.6
Jul	66.7	18.1
Aug	66.4	18.0
Sep	61.9	19.1
Oct	56.4	21.0
Nov	55.0	20.6
Dec	58.7	18.1
DJF	61.6	17.7
MAM	48.4	28.9
JJA	66.5	18.7
SON	58.4	20.0
All seasons	60.3	20.3

Trenberth and Guillemot (1994) show the overall mass balance of the atmosphere and the movement of mass with latitude with the seasons and as the water vapor content of the atmosphere varies. The vertically averaged zonal mean meridional flow associated with the mass redistribution amounts to maxima of 1.6 mm s^{-1} southward in May and 1.5 mm s^{-1} northward in September across the equator (Trenberth et al. 1987).

The data to be analyzed have a large number of grid points and only 17 levels in the vertical. We therefore utilize an alternative method (Hirose and Kutzbach 1969) and algorithm (von Storch and Hannoschöck 1984) for computing the eigenvalues and eigenvectors.

b. The dominant divergent circulations

The analysis was first carried out separately for each month of the year to determine the extent to which the principal components varied. In every case the first two structure functions were remarkably similar, and they were also reproducible in both reanalyses, with minor differences. For the NCEP reanalyses, Table 1 shows the fraction of variance accounted for in each month by the first two CEOFs. For the ECMWF reanalyses (vs NCEP): for January CEOF1 and CEOF2 accounted for 63.0% (vs 62.8%) and 16.0% (vs 16.6%) of the variance.

In July for ECMWF, CEOF1 and CEOF2 accounted for 68.8% (vs 66.7%) and 17.1% (vs 18.1%) of the variance.

As shown in Table 1, typically 75%–85% of the variance is accounted for by the first two CEOFs with a pronounced maximum in the first CEOF in July, and there is a large and statistically significant separation between eigenvalues. A second maximum occurs in January. Thus the first CEOF reveals that the strongest monsoonal circulations occur shortly after the solstice and the values are lowest in the transition seasons. The minimum occurs in March–April.

Because of the strong similarity among the structures that emerged, the analysis was redone with the months combined as seasons—December–February (DJF), etc.—and the results are also given in Table 1. Finally, the results further justified combining all seasons together as an observational matrix four times as big, so that a single vertical structure function was derived for all times of year, but going along with it are four spatial patterns, one for each season. In this case the total variance accounted for by the first CEOF was 60.3% for NCEP, although this also has a seasonal partitioning as given in Table 1.

The vertical structure functions from the NCEP–NCAR and ECMWF reanalyses for the first two CEOFs are given in Fig. 1, and this is constant for all four seasons by design. Figure 2 shows the corresponding four seasonal spatial patterns of the first CEOF (CEOF1) from the NCEP reanalyses and Fig. 3 presents the patterns for COEF2 for just DJF and JJA. Figure 4 shows the same fields for just DJF and JJA for ECMWF.

The vertical structures (Fig. 1) are plotted as vectors, with the arrows free to rotate through 360°. All vectors tend to point either to the left or right, indicating either in-phase or out-of-phase relations and the vectors are so arranged that they can be directly interpreted as showing the large-scale overturning in the upper and lower branches of, for instance, the Hadley circulation. Thus for CEOF1 from NCEP reanalyses, the low-level divergent flow is in one direction below about 400 mb, peaking at 850 mb, but it reverses with height in the upper troposphere to peak at 150 mb, and drops to close to zero by about 70 mb. For ECMWF a very similar vertical structure emerges with the main difference a stronger divergent component near the surface, so the low-level wind maximum is at 925 rather than 850 mb. So this vertical structure applies to the Hadley circulation, but the spatial patterns (Figs. 2, 4) show that the circulation is much broader, varies with longitude, and encompasses a pronounced east–west component as well.

While CEOF1 has an element of familiarity, CEOF2 does not. For CEOF2, the low-level convergence (or divergence) occurs below 800 mb and peaks at 925 mb, while the reverse flow peaks at 700 mb and drops off to nearly zero by 350 mb, indicating a shallow lower-tropospheric overturning. Moreover, it is quite reproducible in both analyses and in all months. However, a

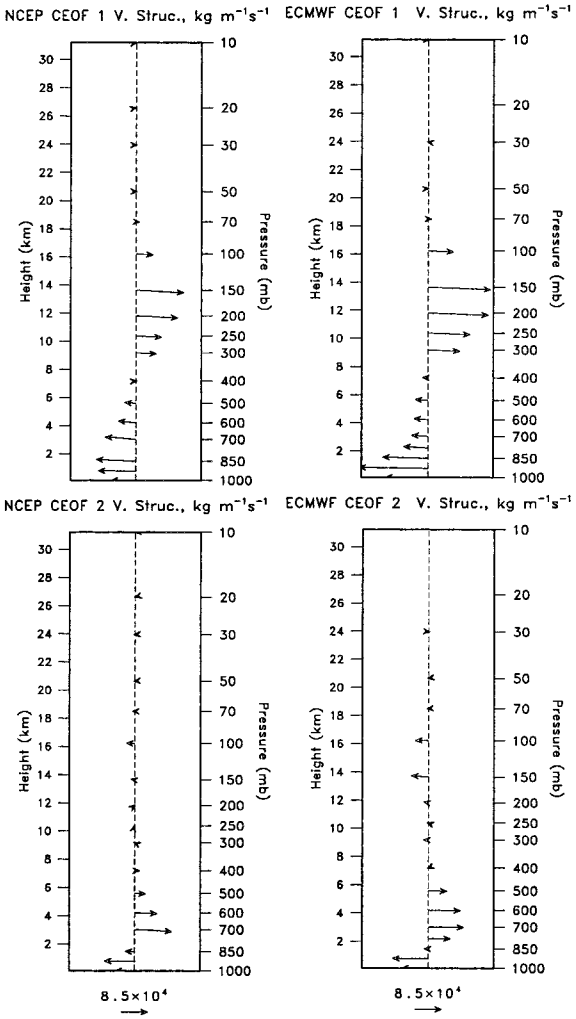

FIG. 1. Vertical structure functions of the mass weighted divergent velocity field from the complex EOF analysis for CEOF1 and CEOF2, from (left) NCEP and (right) ECMWF reanalyses seasonal mean fields for 1979–93. The vectors are referenced to that at 1000 mb, which is directed along the *x* axis; the scale factor is given below; and the units are kg m^{-1} s^{-1}. The vectors are free to rotate through 360° but tend to be aligned. The vertical scale is in mb and with an approximate height scale given.

minor difference between the reanalyses in the CEOF2 vertical structure is a small component at 100 and 150 mb from ECMWF.

In DJF (Fig. 2) the large-scale low-level convergence in CEOF1 and upper-level divergence is most apparent north and east of Australia near 10°S, and the South Pacific convergence zone (SPCZ) is clearly a part of this pattern. In the Indian Ocean the ITCZ is also evident near 10°–15°S. Similarly, strong low-level convergence occurs over the Amazon while the subsidence over the tropical eastern Pacific is present as the downward branch of the Walker circulation. The latter is slightly stronger relative to the Hadley circulation in the NCEP reanalyses, as is readily apparent from the spatial structures. However, the vertical structure function has slight-

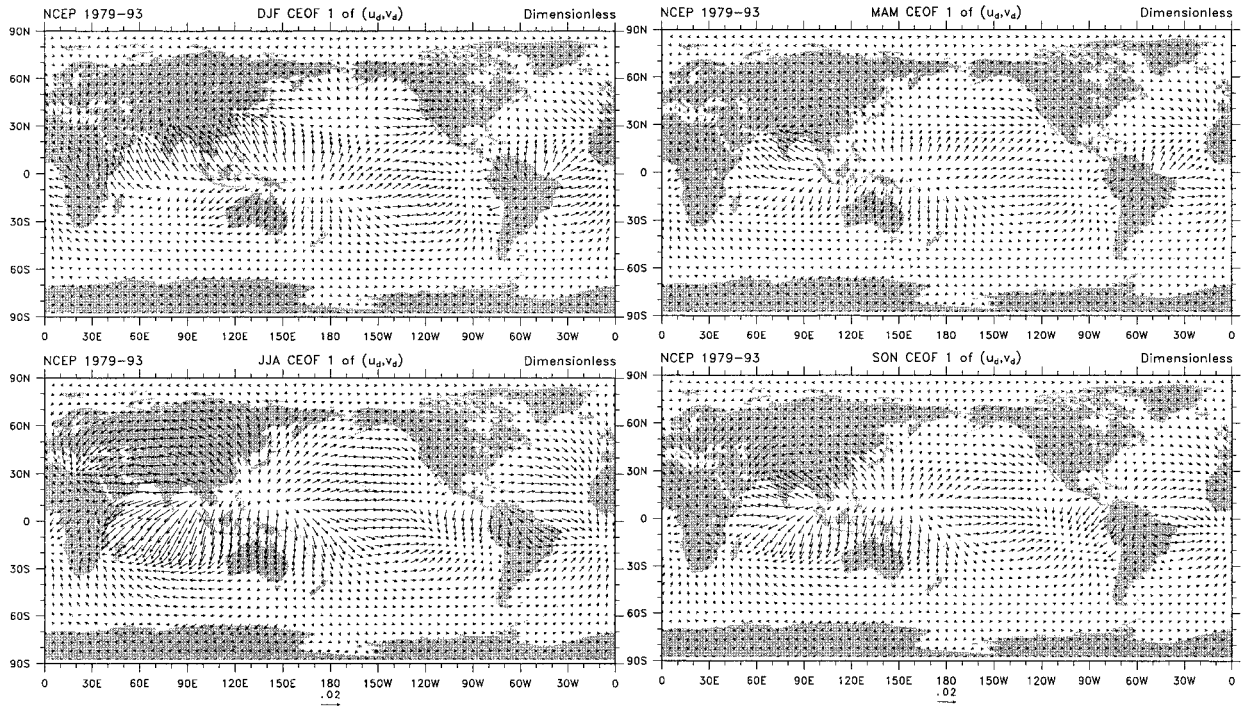

FIG. 2. Spatial patterns of the divergent velocity from NCEP reanalyses for CEOF1 where all four seasons are combined (60.3% of the variance) for DJF, MAM, JJA, and SON, corresponding to the vertical structure function in Fig. 1. The scale vector is given below.

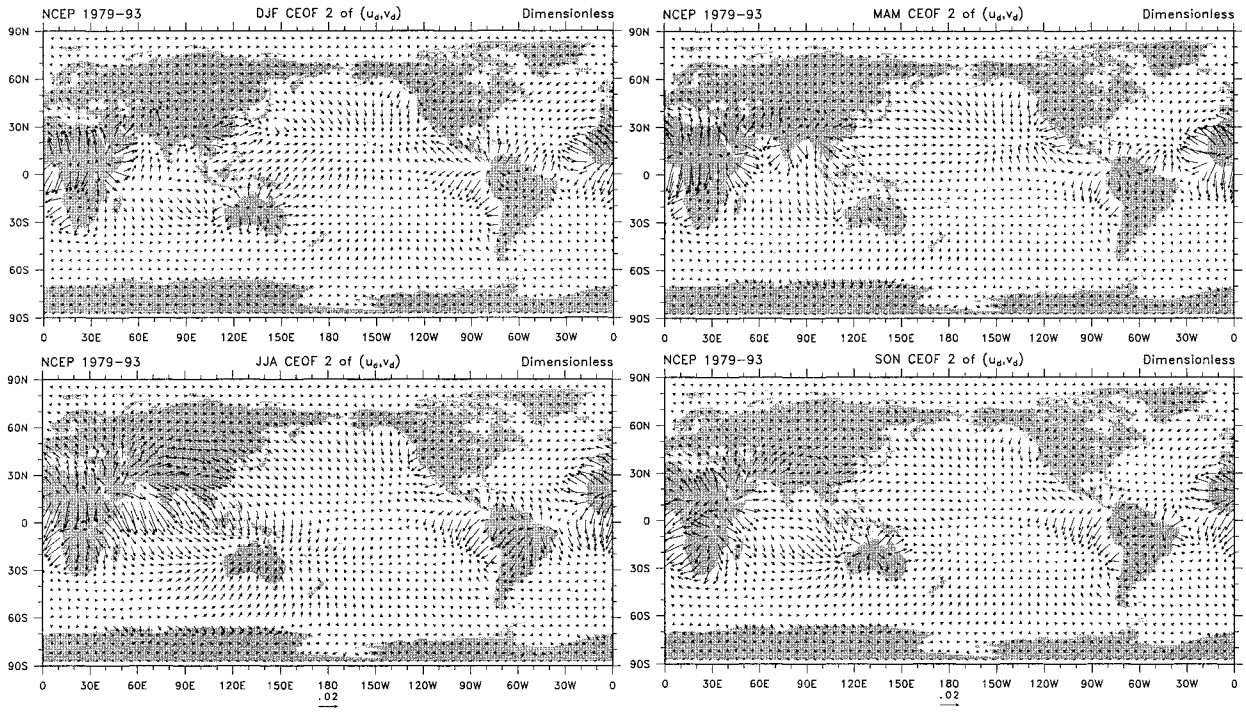

FIG. 3. Spatial patterns of the divergent velocity from NCEP reanalyses for CEOF2 where all four seasons are combined (20.3% of the variance) for DJF, MAM, JJA, and SON, corresponding to the vertical structure function in Fig. 1. The scale vector is given below.

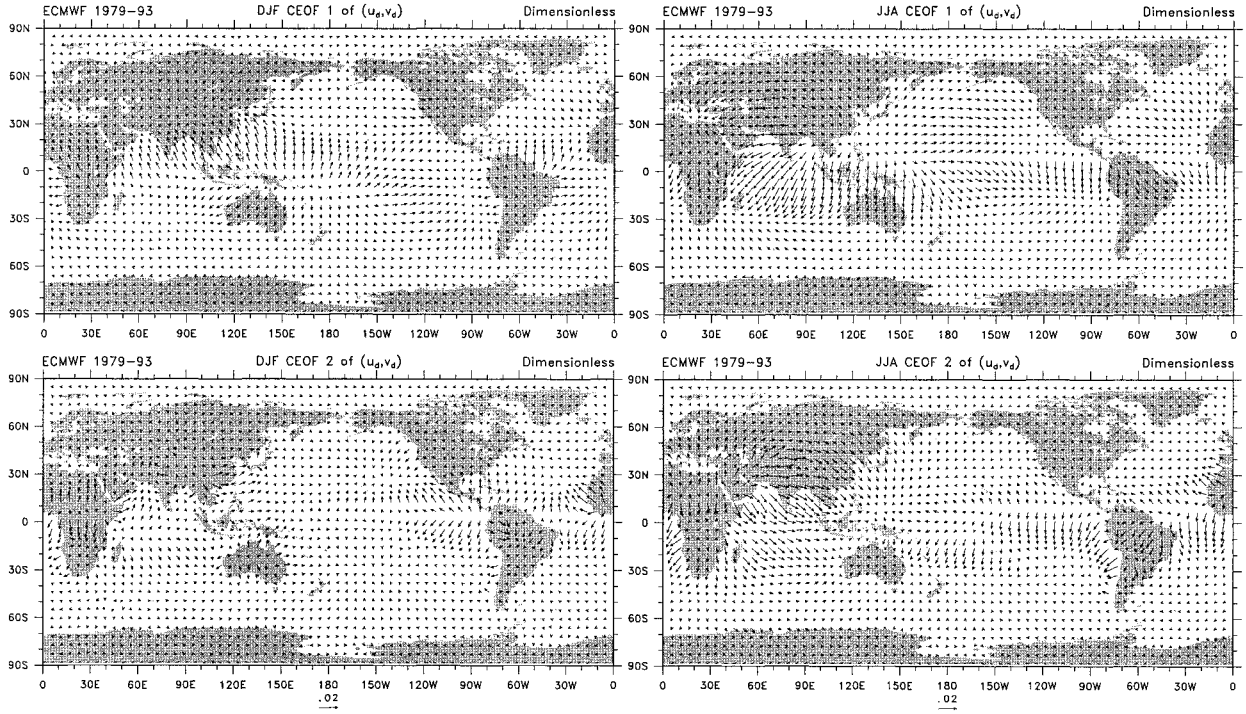

FIG. 4. Spatial patterns for (top) CEOF1 and (bottom) CEOF2 from ECMWF reanalyses for the analysis where all four seasons are combined and correspond to the vertical structure function in Fig. 1. The vectors indicate the divergent velocity, with the scale vector given below for (left) DJF and (right) JJA.

ly larger values in the ECMWF reanalyses. This multiplicative factor means that it is the stronger Hadley component in the ECMWF reanalyses (section 5) that makes up the more significant difference. This can be seen better in the corresponding vertical motion fields (presented in Fig. 5). In DJF strong subsidence is also evident into the North Pacific subtropical high. A distinctive line of convergence in the upper troposphere occurs from 90°E to 170°W along about 30°–35°N, penetrating farthest north near Japan, which bears a striking resemblance to the position of the core of the subtropical jet stream where it exceeds 50 m s^{-1} in January. A primary forcing of the rotational zonal wind component comes from the term $f\upsilon_d$, where υ_d is the divergent meridional wind component and f, the Coriolis parameter, increases northward, so that this term reaches a maximum just short of the convergence line. Not all of the subtropical jet has this linkage, however, as this relationship is missing in the jets over the southeastern parts of the United States and the Middle East.

While some low-level convergence is apparent in CEOF1 in the southern Tropics over Africa, the main features over Africa and Australia are accounted for by CEOF2. Thus the shallow overturning is an important component over these two continents in the reanalyses, with convergence near 10°N over Africa, subsidence over the Sahara and tropical Atlantic, convergence over Australia, and convergence near Colombia, in South America, and over the eastern Pacific. The distinctive pattern in CEOF2 off the west coast of South America may be partly brought about by ringing effects from the Andes and is not fully reproducible in detail. However, the overturning circulations involving the ITCZs are not fully represented by CEOF1 and CEOF2.

The MAM patterns are similar but weaker than for DJF, and the Southern Hemisphere (SH) convergence migrates closer to the equator, so that by JJA, the southeast Asian monsoon dominates CEOF1. The outflow is predominantly into the SH to the core of the subtropical jet-stream. The main upper-tropospheric convergence occurs from 60°E across Australia to the date line where the jet exceeds 40 m s^{-1} at 200 mb in July. The extension of the subtropical jet into the Pacific is not so clearly linked with upper-level meridional overturning winds from the north, however. Over Africa and the Arabian Sea in JJA CEOF2 dominates, as the low-level convergence moves northward with maximum convergence near 20°N and just south of the equator. In SON the patterns are more like those in JJA than other seasons, but the main low-level convergence has moved from 15°–20°N to about 10°N. In all seasons the Hadley component is relatively greater than the east–west component in the ECMWF reanalyses.

The CEOF1 results, in particular, illustrate that overturning is important in the zonal direction as well as north–south. Accordingly, these aspects are examined further in sections 4 and 5.

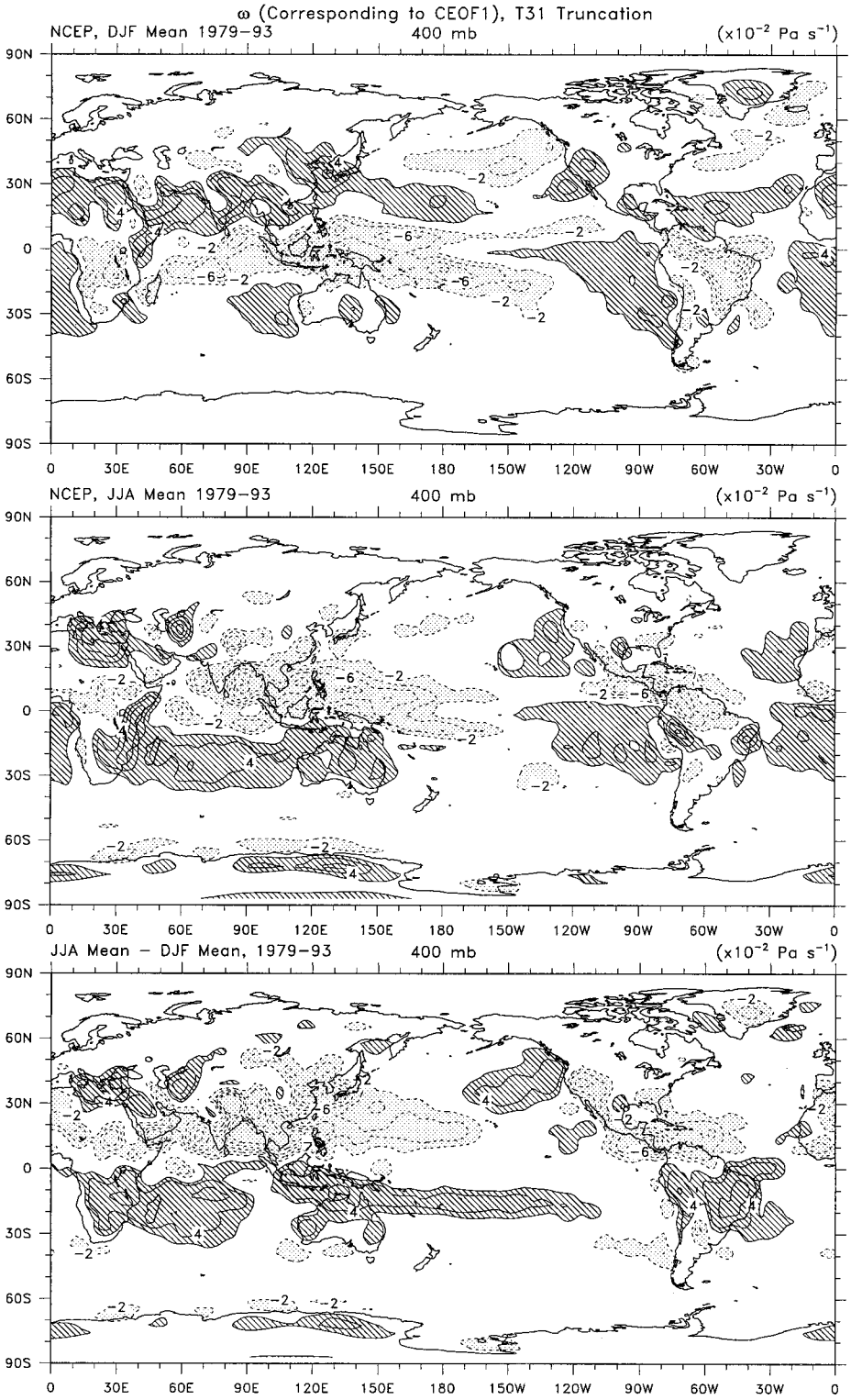

FIG. 5. Vertical p velocity ω at 400 mb for CEOF1, contour interval 2×10^{-2} Pa s^{-1} for the seasons DJF and JJA, and their difference JJA−DJF. The zero contour has been omitted for clarity. Negative values are stippled and positive values are hatched (negative means upward motions in the top two panels). Fields are smoothed to T31 truncation.

c. The vertical motion fields

The vertical motion fields corresponding to the CEOF patterns were obtained by integrating the equation of continuity $\nabla \cdot \mathbf{v} + \partial\omega/\partial p = 0$ from the top downward. For CEOF1 this was integrated downward to 350 mb, giving ω at 400 mb, and for CEOF2 the integration was to 775 mb for NCEP and 800 mb for ECMWF (owing to the extra 775-mb level in the ECMWF reanalyses), giving values of ω at about 800 mb.

The resulting ω fields are given in Figs. 5 and 6 for the NCEP reanalyses for CEOF1 and CEOF2, for DJF and JJA. The main differences with ECMWF are the much stronger ITCZs in the eastern Pacific and Atlantic, as revealed by the annual means (Fig. 7). To confirm the degree of agreement, spatial correlations between the NCEP and ECMWF results have been computed over the global domain for the ω fields for both CEOFs. For CEOF1 these are 0.88, 0.82, 0.87, and 0.86 respectively for DJF, MAM, JJA, and SON, while for CEOF2 they are 0.80, 0.81, 0.68, and 0.76. The seasonal differences implicit in the concept of the monsoon are highlighted by the differences between DJF and JJA in Fig. 5.

The mean fields in Fig. 5 are quite similar to the average total ω fields at 400 mb (not shown). Figure 5 shows the eastern Pacific ITCZ, the large-scale migration of the predominant rising motion across the equator with the seasons and the enhancement of activity in the SPCZ in DJF. The pronounced subsidence in the South Pacific high is present all year, while the subtropical high in the North Pacific is much stronger in summer. The migration across the equator of the upward motions is evident in Africa and from the Amazon region to the Mexican highlands. In the NCEP fields the Atlantic ITCZ is weak except where it links to the South American monsoon, although this is not the case in the ECMWF fields.

The seasonal changes in vertical motion (Fig. 5) are most pronounced from 35°S to about 50°N. In the Northern Hemisphere, the large changes in extratropical storm track activity are reflected in the figure along with the monsoonal changes, which are especially evident throughout the Eastern Hemisphere, extending into the central Pacific and over the Americas.

For CEOF2 (Fig. 6) the zero contour is omitted to highlight the regions where this mode is more important, namely, over Australia, Africa, and the eastern Pacific and Atlantic. Over the tropical continents, there is a prevalence of upward motion with the corresponding sinking over immediately adjacent waters. The exception is Australia in JJA, which is when wintertime cooling is sufficient to favor a strong subtropical anticyclone. The eastern Atlantic and Pacific ITCZ regions are also evidently where low-level upward motions are enhanced, with the subsidence over the subtropical oceans to the north and south. As for CEOF1, the main differences between the NCEP and ECMWF CEOF2 ω fields are the stronger features in the eastern ocean ITCZs (not shown).

d. Links to precipitation

To illustrate the connection between primarily the first CEOF mode and the precipitation, Fig. 8 shows the mean precipitation estimates from Xie and Arkin (1997) (called the Climate Prediction Center Merged Analysis of Precipitation) along with the divergent wind component at 200 mb for January and July. There is excellent agreement qualitatively between the regions of average precipitation in the Tropics and subtropics and upper-tropospheric divergence. This is true not only for the major rainfall areas, but also for narrow features like the ITCZ over the Pacific and Atlantic, and over Africa. Even the main storm track regions in the extratropics, where the precipitation presumably mainly arises in transient baroclinic storms, there is a small signature of upper-tropospheric divergence such as in the North Pacific and North Atlantic in January and in the South Pacific from 30° to 40°S in July. The latter is the extension of the SPCZ into the extratropics where it tends to form a ''graveyard'' for eastward migrating fronts. The precipitation band from the storm track at higher latitudes is not reflected in the mean upper-tropospheric outflow. This figure also allows the 200-mb divergent flow to be compared with that implied for CEOF1 in Fig. 2 for DJF and JJA and, more specifically, for January and July (not shown). While broadly similar, some features are noticeably different, especially over Africa. While the migration of the African monsoon rains from 0°–20°S in January to 0°–20°N in July is seen at 200 mb as an upper-tropospheric divergence, it is less distinctive in CEOF1, and CEOF2 clearly plays a role there.

4. East–west circulations

For the equatorial bands, such as from 10°N to 10°S, upward motion prevails at most longitudes, while from 15° to 30° latitude downward motion is predominant. Accordingly, to better indicate the east–west overturning aspects, it is desirable to span the latitudes of the Hadley circulation. Figure 9 presents the mean divergent zonal circulation for 90°N–90°S for January and July, at the times of the extremes. For the region 30°N–30°S the picture is quite similar, except the values are about two times bigger, although there is a notable difference in one location in January. In particular, differences are substantial between 90° and 150°E, where the subsidence evident in the global picture is not present from 30°N to 30°S. In July the two regions indicate almost identical results. As Fig. 9 is for the global domain, the circulations must be closed and a streamfunction can be computed; see appendix. At low levels, below about 700 mb, both the vectors and the mass streamfunction are perturbed by high topographic ef-

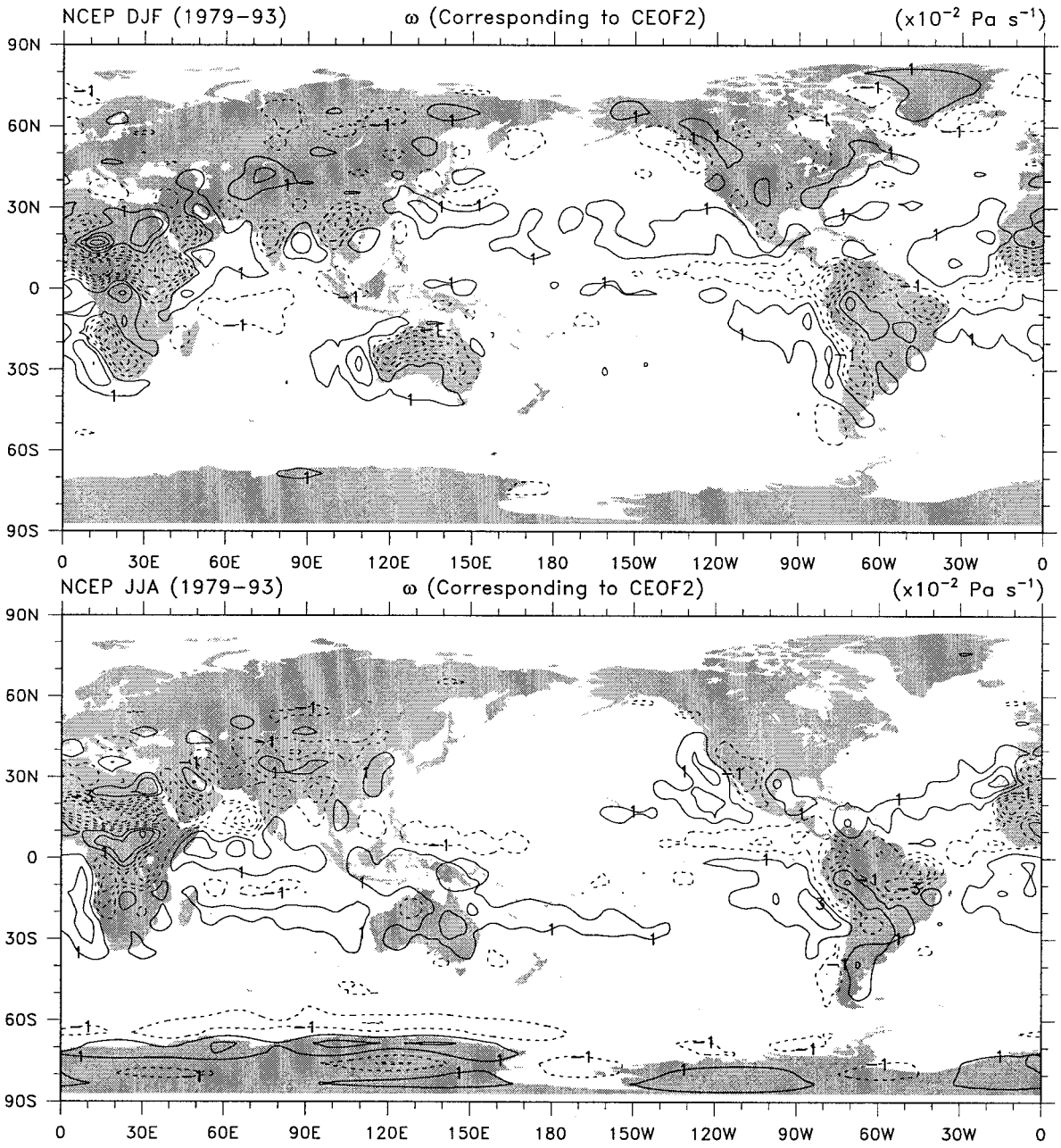

FIG. 6. ω at about 800 mb for CEOF2, contour interval 2×10^{-2} Pa s^{-1}, for DJF and JJA. Note that the contours plotted are odd and there is no zero line. Negative (upward) motions are dashed. Fields are smoothed to T31 truncation.

fects, especially from Antarctica, the Himalayan–Tibetan plateau, and the Andes–Rockies. Thus in Fig. 9, the streamfunctions were computed downward to 850 mb and linearly interpolated to a zero value at 1000 mb, to partially overcome the spurious topographic effects (see appendix).

Therefore the global picture in Fig. 9 arises mostly from the 30°S–30°N domain. This figure illustrates the prominence of the east–west overturning. For the global domain the overturning mass fluxes exceed 50×10^9 kg s^{-1} (NCEP) in January and over 100 units in July and are fairly comparable to the mass fluxes in the Hadley cells (section 5).

Both globally and for the extended Tropics, the predominant transverse circulations occur in three regions that move somewhat with the seasons. The first consists of rising motion from 150°E to 180° in January and from 80° to 140°E in July, a transverse circulation to the west, and subsidence from 100° to 130°E in January (mainly into the Indian Ocean subtropics south of the

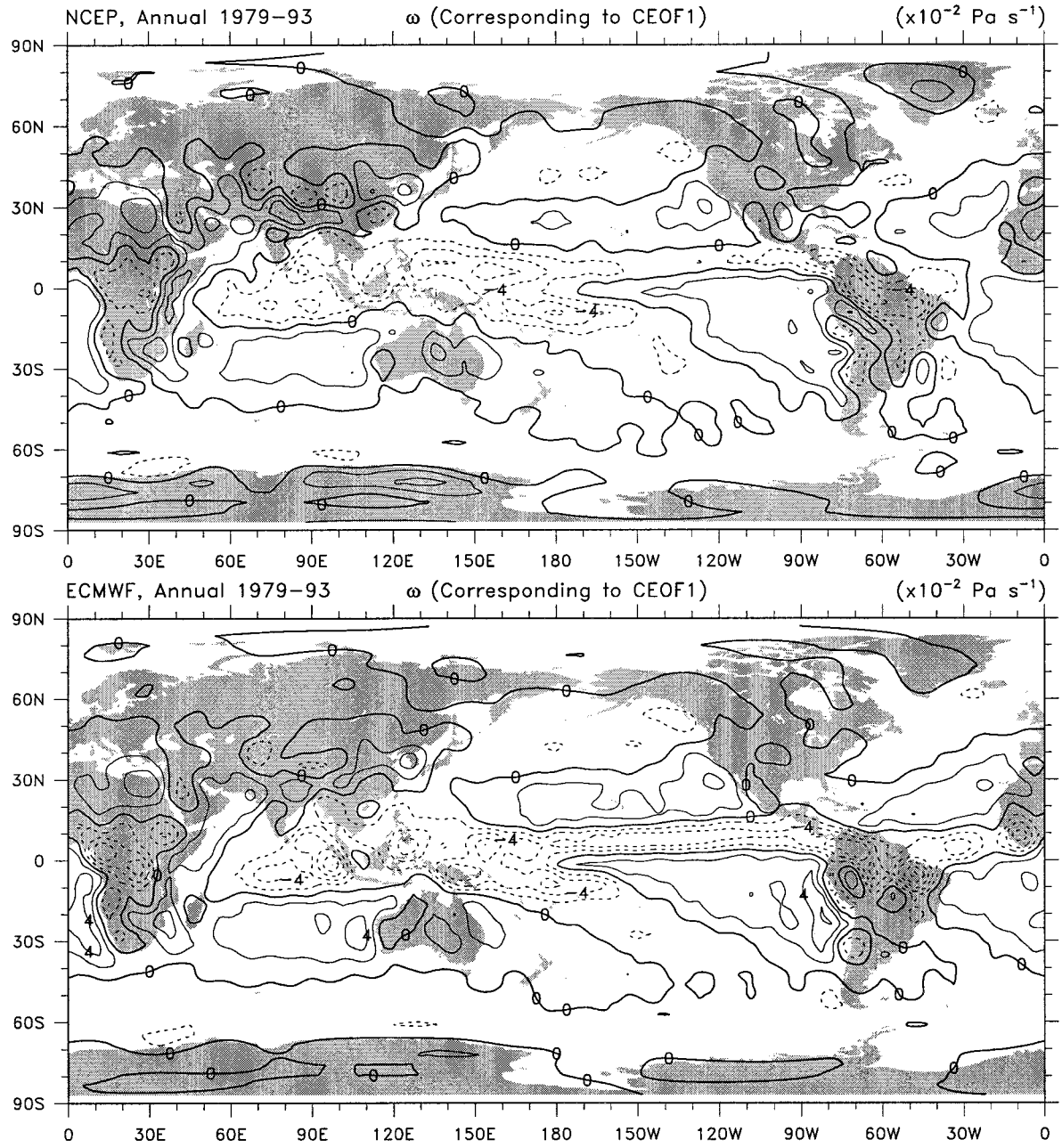

FIG. 7. Annual mean ω at 400 mb for CEOF1 from NCEP and ECMWF, contour interval 2×10^{-2} Pa s^{-1}. Negative (upward) motions are dashed. Fields are smoothed to T31 truncation.

equator) and 0° to 70°E in July (into the subtropical Indian Ocean south of the equator and the Mediterranean). The second is the Pacific Walker circulation, which is strong in January when the SPCZ is most active. The third is another Walker-type circulation in the Americas–Atlantic sector that moves from being centered at 20°W in January to 45°W in July, as the predominant action moves from south of the equator in January to north of the equator in July.

5. The zonal mean circulation

a. The Hadley cells

It is apparent from Figs. 2–4 that the Hadley circulation is a major part of the large-scale overturning in the atmosphere, and so zonal mean cross sections of the mass meridional streamfunction show many of the features. Figure 10 therefore shows a four-panel figure of the mean meridional circulation climatology from

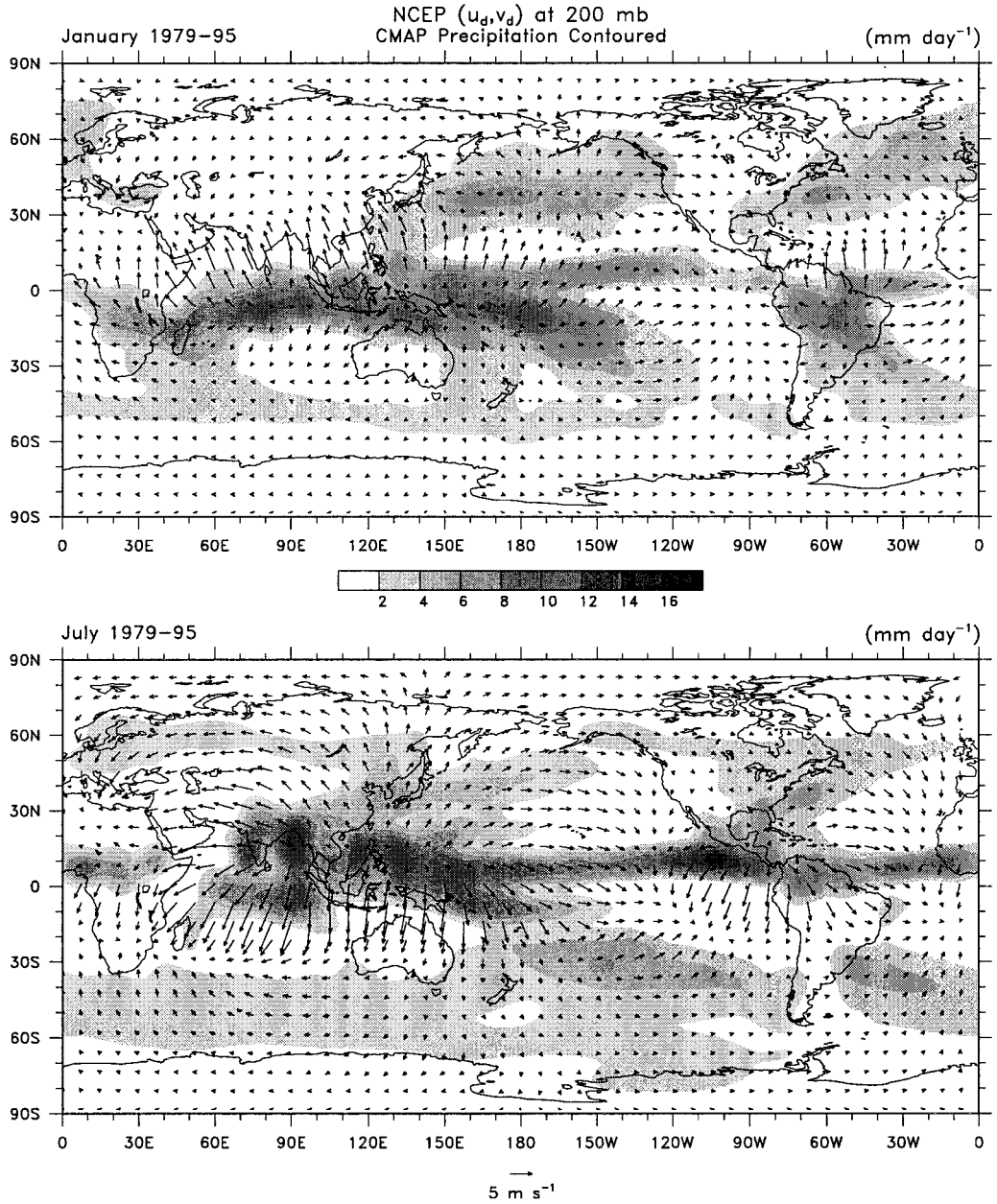

FIG. 8. For 1979–95, mean precipitation in mm day^{-1} from the CMAP analysis along with the NCEP 200-mb divergent wind component in m s^{-1}, with the scale vector below each plot for Jan and Jul. The grayscale increments in 2 mm day^{-1} and values less than 2 mm day^{-1} are left blank.

NCEP reanalyses for January, April, July, and October to reveal the mean annual cycle. The corresponding results from ECMWF are presented in Fig. 11. There are two Hadley cells and the dominance switches from one hemisphere to the other with the seasons. Note that this depiction clearly shows more vertical structure than perceptible from CEOF1, as there is often a small lower-level mass circulation that evidently comes from CEOF2.

The peak mass flux in each Hadley cell at 400 mb for each month, fitted with a smoothing spline, is plotted in Fig. 12 for both reanalyses. Differences in magnitudes are small in the Northern Hemisphere (NH) although the shape differs enough that the broad summer minimum peaks in different months. In the SH, the annual cycle is similar but the ECMWF values are 20% or so larger. Also, from Fig. 10 it is evident that for ECMWF the maximum Hadley cell mass flux often occurs about 700 mb in association with the lower-troposphere cell. For the deep Hadley circulation the strongest cell is in

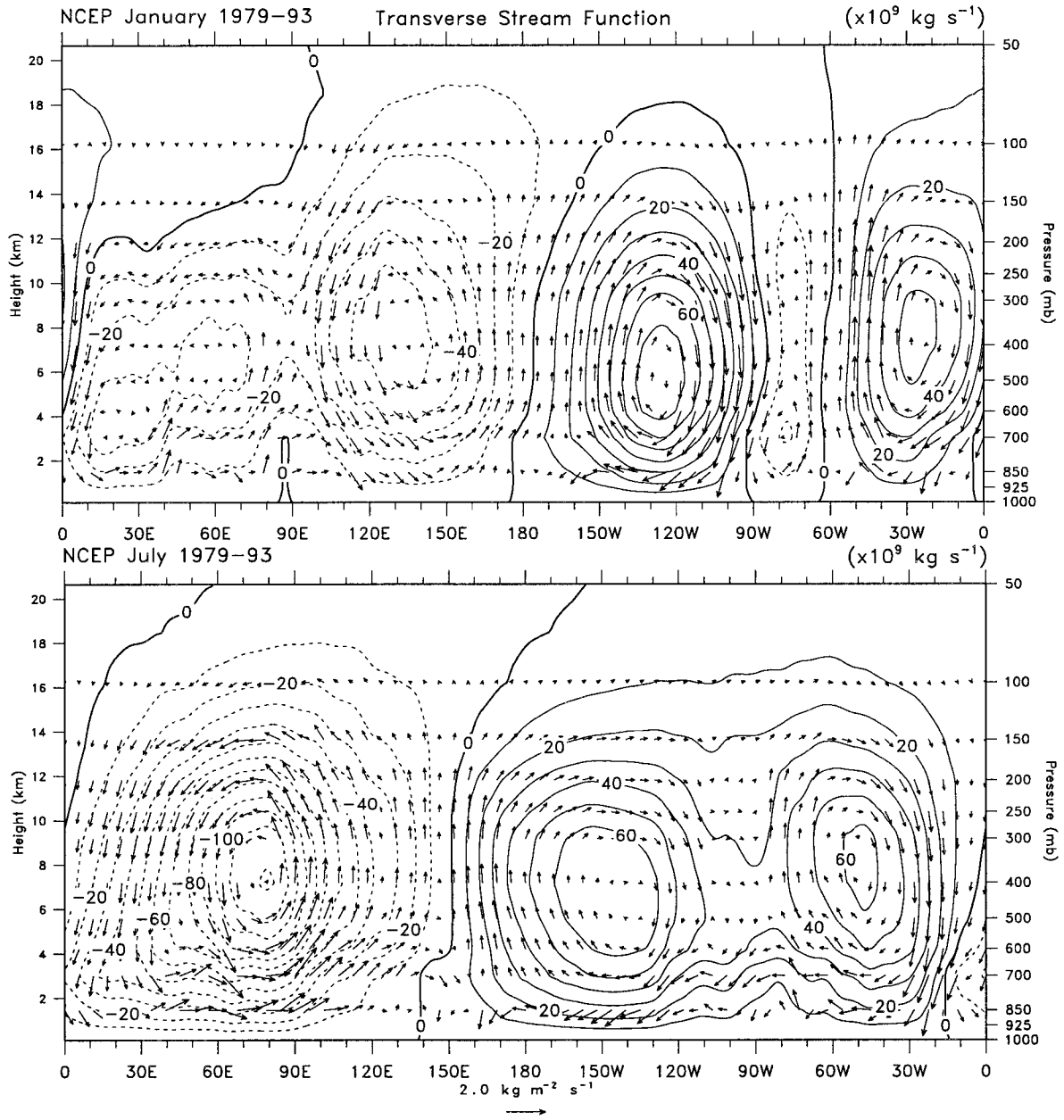

FIG. 9. The mean divergent east–west mass circulation for Jan and Jul from NCEP reanalyses averaged from 90°N to 90°S. The reference vector indicates the mass flux in kg m^{-2} s^{-1} and the mass streamfunction is contoured in 10×10^9 kg s^{-1}.

the SH in July–August, peaking in early August at 180 $\times$ 10^9 kg s^{-1} (NCEP) or 220 units (ECMWF) and waning to about 30 units in January. In the NH the cell is strongest in late January to early February at -170 to -180 units, and this cell becomes very weak in the northern summer JJA. The migration of the strongest zonal mean upward motion back and forth across the equator from 10°N in JJA to 10°S in DJF reflects only part of the strong regional migration that is much more extensive. Over the Pacific and Atlantic Oceans, the ITCZ remains in the NH year-round, and, although these features are not easily seen in Fig. 2, they clearly add to the strength of the southern Hadley cell in JJA and detract from the zonal mean in DJF.

b. The Ferrel cells

The indirect Ferrel cells in midlatitudes lie between about 30° and 60°. For NCEP, the Ferrel cell is centered near 650 mb and the low-level flow is concentrated nearer the surface than in the ECMWF reanalyses, where the center of the mass circulation is more like

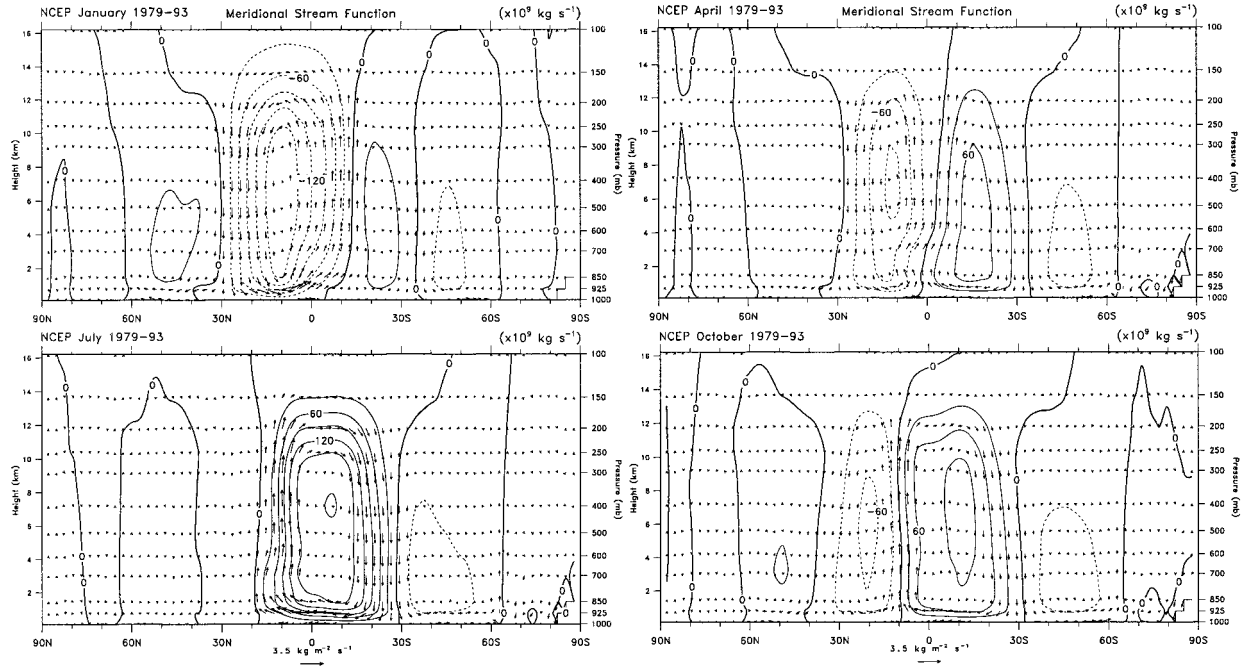

FIG. 10. NCEP zonal mean meridional circulation as vectors, scaled to the two axes to represent the true direction and magnitude, and mass flux streamfunction, contour interval 30×10^9 kg s^{-1} for mean from 1979–93 Jan, Apr, Jul, and Oct.

600 mb. A comparison of the annual cycle of the Ferrel cell mass flux is reasonably represented by values at 700 mb (Fig. 12). Note that the hemispheres are switched in the figure compared to the Hadley cell, because of the reversal in cell direction. In both hemispheres the ECMWF Ferrel cell is stronger as well as more extensive vertically, and the difference is especially great in the Southern Hemisphere above 600 mb. The profiles of the annual cycles are quite similar in the two analyses, however. The Ferrel cell is remarkably

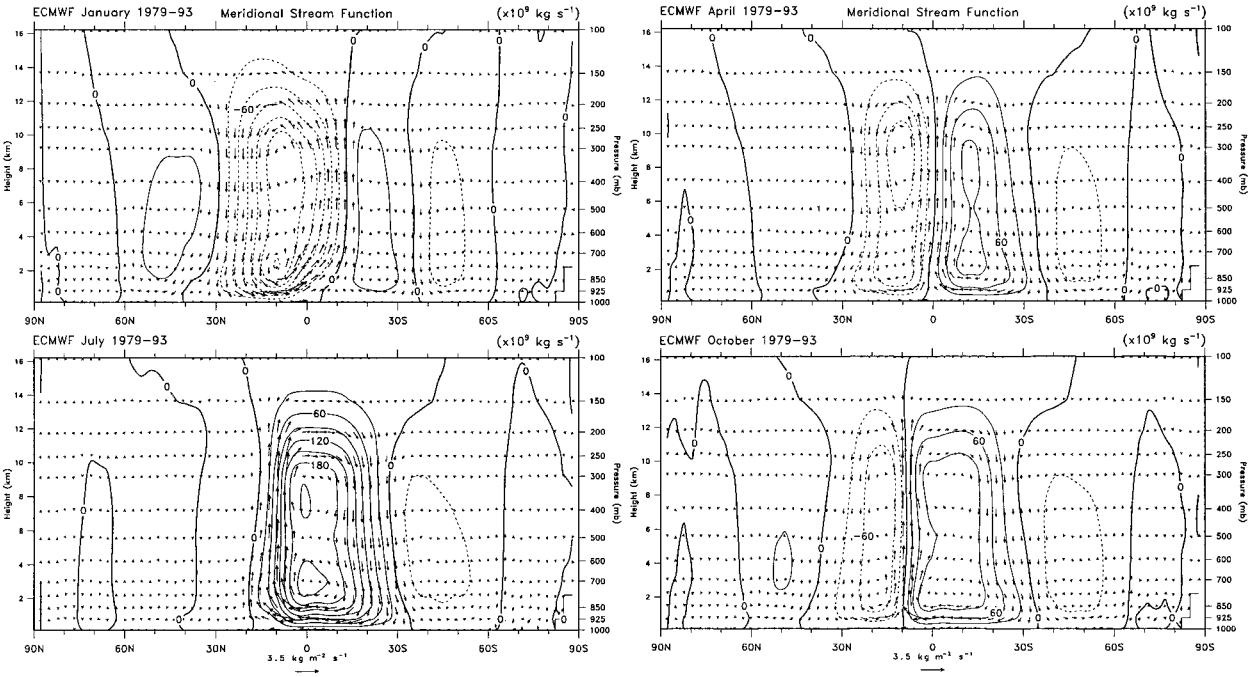

FIG. 11. ECMWF zonal mean meridional circulation as vectors, scaled to the two axes to represent the true direction and magnitude, and mass flux streamfunction, contour interval 30×10^9 kg s^{-1} for mean from 1979–93 Jan, Apr, Jul, and Oct.

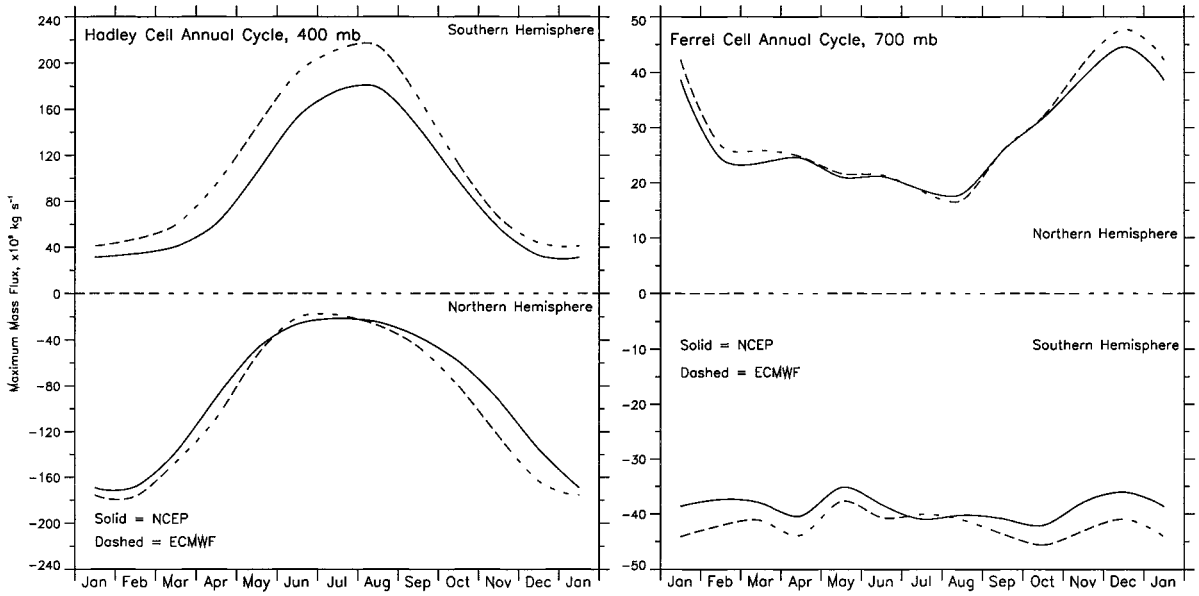

FIG. 12. Annual cycle of the maximum mass flux in the two Hadley cells at 400 mb (left) and the Ferrel cells at 700 mb (right) in 10^9 kg s^{-1} from NCEP (solid) and ECMWF (dashed).

constant in amplitude throughout the year in the Southern Hemisphere at about 40×10^9 kg s^{-1}, while in the north there is a broad minimum from about February to September, and a fairly sharp maximum in December.

c. The vertical motions

Given the results from the CEOF analysis, it is apparent that the level of nondivergence is somewhat above 500 mb for the dominant CEOF1 mode. However, much of this mode can be reconstructed simply by examining the vertical motions through 500 mb. Also, using the ω fields facilitates a comparison between the analyses from NCEP and ECMWF that, for the zonal means, is shown in Fig. 13. The first point to note is the remarkable agreement between the results from the two centers both in terms of the annual cycle evolution and the magnitude of the values. Largest differences appear south of 60°S where the database is weakest.

Upward motions are strongest about 10°N in August but with a gradual weakening through to February as this upward branch moves slightly southward. A separate upward branch appears south of the equator about September near 5°S and intensifies and moves farther south to reach a peak in February at 10°S. Meanwhile, in the subtropics there is a pronounced annual cycle in subsidence peaking at 25°N in February and 30°S in August. The upward branch of the Ferrel cells are seen year-round around 60°N and 65°S. A secondary subsidence region occurs at 40°N about September.

6. The steadiness of the monsoon circulations

In dealing with the monsoons, there is an implication that the thermally driven large-scale overturning circulation is dominant over the transient daily variations. Ramage (1971) notes that a fundamental property of the monsoons is their persistence until they change from the summer regime to the winter regime and vice versa. Yet increasingly attention is being paid to the monsoon ''breaks'' and transients are identified on various timescales. The latter are often broken up into diurnal, less than 5 day, 1–2 weeks, or intraseasonal Madden–Julian oscillations that have periods attached to them of 30–60 days [see Webster et al. (1998) and Annamalai et al. (1999) for some discussion]. In addition, a pronounced diurnal cycle exists in the Tropics but, as it is forced, it should be treated separately from other frequency bands in determining transients.

We use the ω field at 500 mb to examine the steadiness issue. As this deals only with the divergent circulation, whereas a major part of the monsoon circulation is rotational, the results are likely to be an overestimate of the importance of the transients relative to the mean flow. Accordingly, we are flexible in the criteria adopted to determine the steadiness.

We compare the daily mean of values at 0000, 0600, 1200, and 1800 UTC, which provides a reasonable measure of the transients, with the seasonal mean $\overline{\omega}$. While taking the daily average removes more of the variance than just the mean diurnal cycle, some of the high-frequency variability is spurious because it arises from changes in the observing system throughout the day. Thus we compute the ratio of the mean flow $\overline{\omega}$ to the sample standard deviation $s(\omega)$ of daily averages of ω as a signal-to-noise ratio. The inverse of this is called a coefficient of variation, but it is troublesome to deal with where the mean is small or zero. However, as the

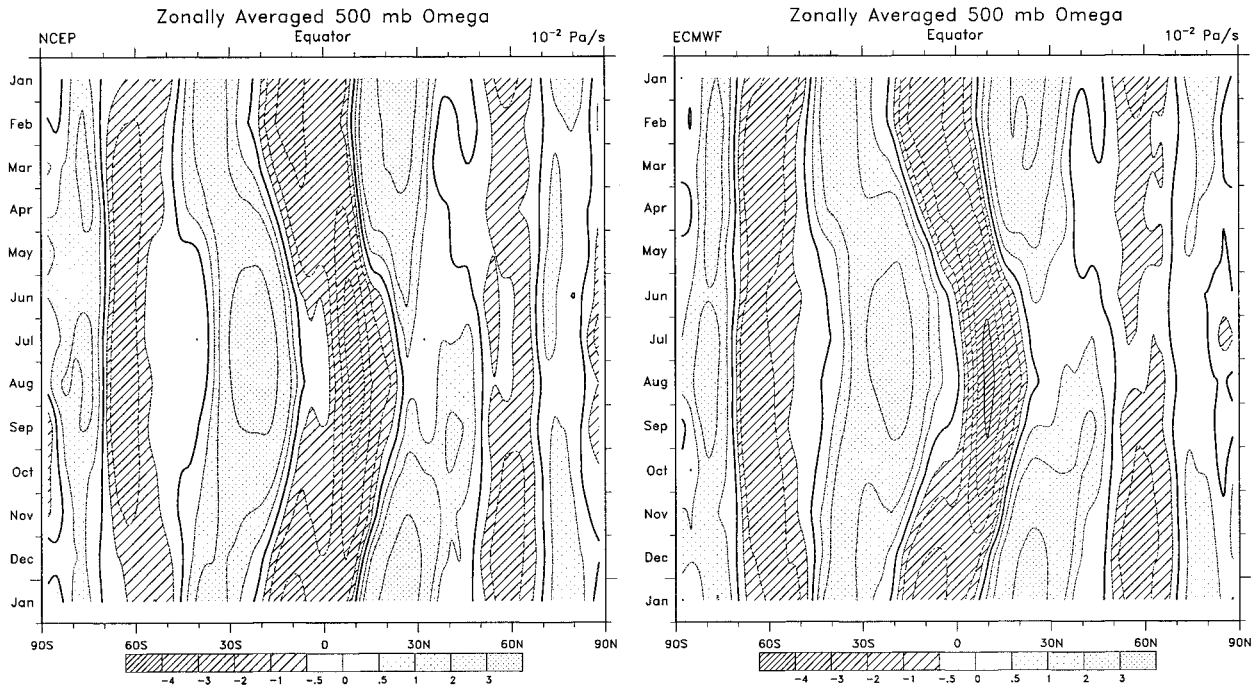

FIG. 13. Annual cycle of the zonal mean ω at 500 mb from (left) NCEP and (right) ECMWF in 10^{-2} Pa s^{-1}. Hatching indicates upward motion and stippling subsidence. Note the uneven contour interval.

standard deviation is positive definite, defining the ratio in this way causes no such problems.

There are distinctive regional differences in the $\overline{\omega}$ from NCEP and ECMWF (not shown), most notably in the vicinity of topography. Also of note is weaker upward motion in the Pacific ITCZ in the ECMWF reanalyses in DJF at 500 mb (but not at 300 mb). Of greater note is the considerably greater daily variability in the ECMWF analyses, as shown for DJF in Fig. 14, and similar results occur for other seasons. NCEP variability is much lower throughout the SH, over South America and the tropical Pacific, and over the North Pacific storm track region. Differences over South America and the western and central tropical Pacific are about 0.05 Pa s^{-1}, which is as large as the values themselves.

Accordingly, the monsoon signal-to-noise ratios are generally larger for the NCEP reanalyses. However, as the overall patterns are quite similar, we present only the NCEP results for DJF and JJA seasons (Fig. 15). In this figure magnitudes exceeding 0.6 are stippled. The areas where the signal-to-noise ratio is >1 are quite small. We performed the identical analysis with 5-day ω averages, so that the $\overline{\omega}$ is unchanged but the noise is somewhat less. The patterns are very similar but with the 1.0 contour corresponding roughly to the 0.6 contour in Fig. 15. Therefore an interpretation of the 0.6 contour is that it corresponds to where the seasonal mean signal is either on a par with that of 5-day variability or 60% of the one-day variability.

Autocorrelations of daily ω (not shown) are typically $\sim$0.5 throughout the Tropics and exceed 0.7 locally. Thus in the Tropics, the characteristic decorrelation timescale for variability is 3–5 days. In midlatitude storm tracks, on the other hand, the one-day autocorrelations are negative. By normalizing the $\overline{\omega}$ by the standard deviation, the values in the extratropics are naturally diminished in magnitude owing to the larger daily variance associated with midlatitude Rossby waves. However, the daily variance drops in polar regions and the signal-to-noise ratios also have some maxima over Antarctica and Greenland, which are important orographically but of less interest here.

Using the large-scale features in Fig. 15 with values exceeding 0.6 as indicators, the dominant persistent features with seasonal migrations are the rising motions over (a) the tropical western and central Pacific and the eastern tropical Indian Ocean; (b) Central and northern South America; and (c) Africa; while the main subsidence regions are (d) the tropical and subtropical southeast Pacific; (e) the tropical and subtropical southeast Atlantic, which extends over southern Africa in JJA; (f) North Africa and the Middle East; (g) the subtropical North Pacific (more so in JJA); and (h) the subtropical Indian Ocean. The same features are identifiable in the ECMWF results. The most stable and persistent feature of the circulation year-round is the South Pacific high (values exceed $+1$ both seasons). However, the strongest persistence seasonally in the vertical motions occurs in the rising motions over the

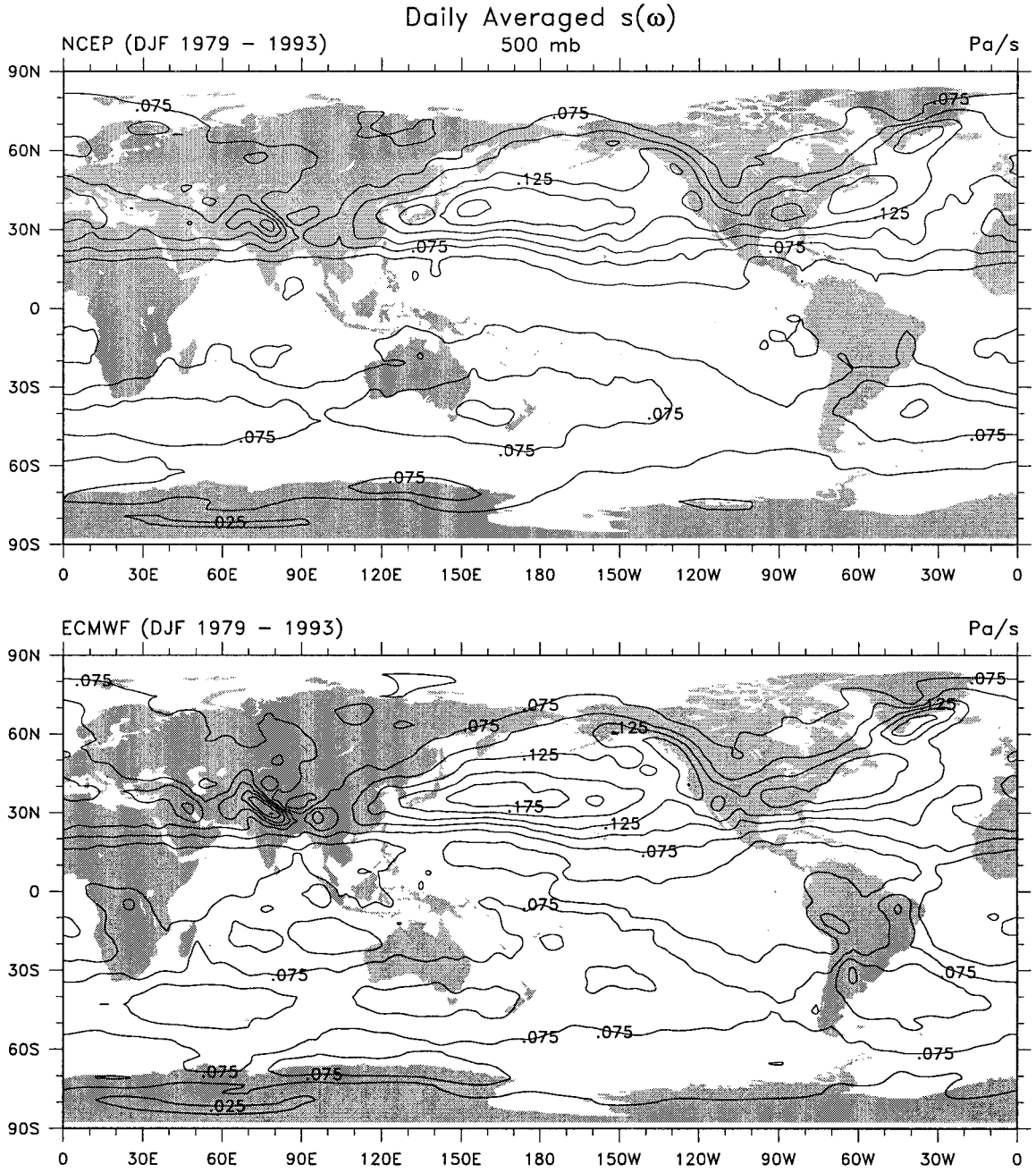

FIG. 14. Standard deviation of daily average 500 mb ω, $s(\omega)$, for DJF from (top) NCEP and (bottom) ECMWF. The contour interval is 0.025 Pa s^{-1}.

Amazon in DJF, which moves to central America in JJA (both with values exceeding -2), and the subsidence over the Mediterranean and north and east Africa in JJA.

Accordingly, this analysis successfully depicts the main monsoon regions, although it should be realized that the transient fluctuations from day to day contain more of the variance than the seasonal mean.

7. Regional monsoons

Six regions have been selected to illustrate and highlight meridional structures of the overturning monsoonal circulations. Here we use the ECMWF results because the extra 775-mb level proves quite beneficial and the flow at 925 mb is more distinctive. The sections, progressing eastward, were selected from a larger subset

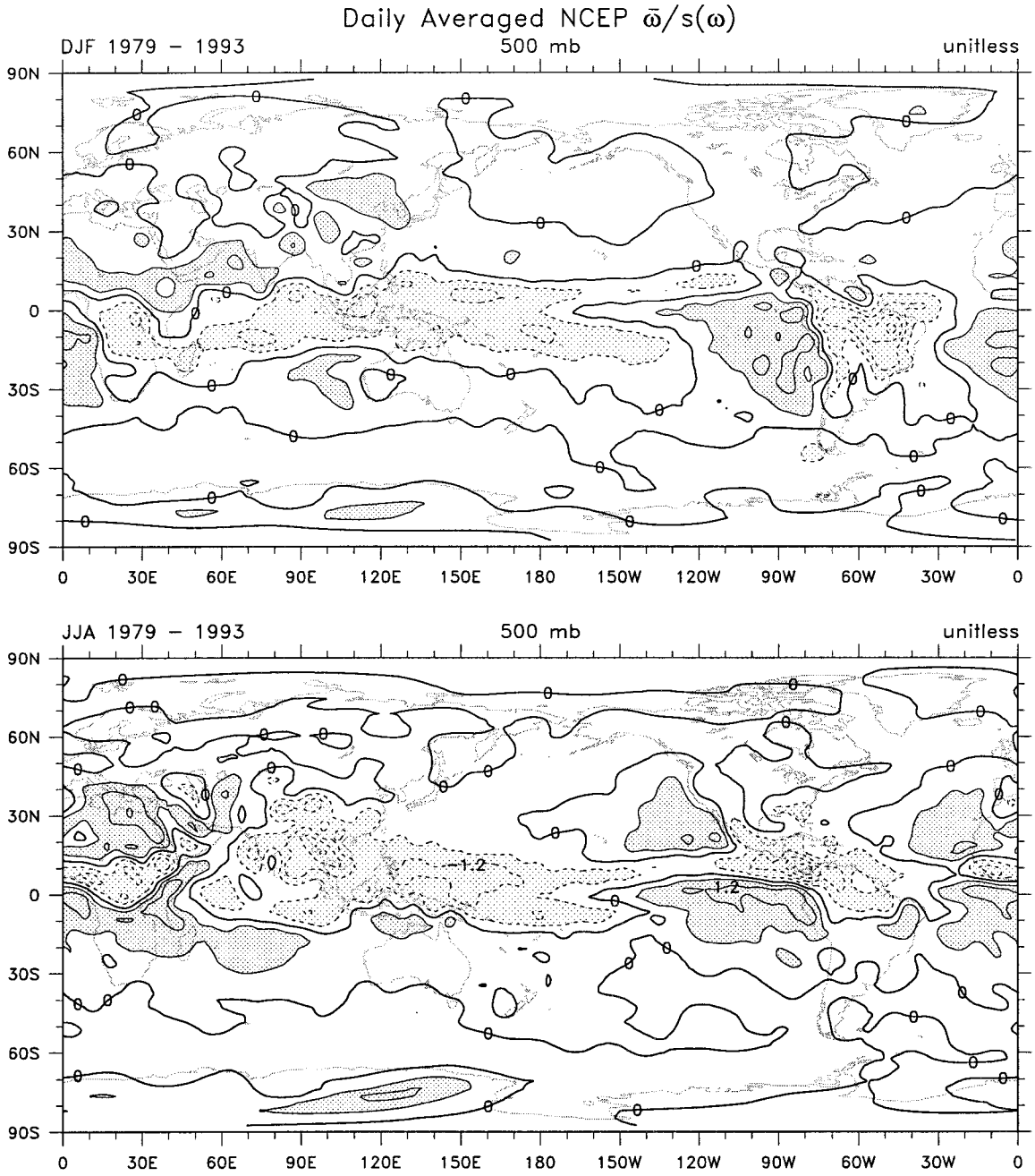

FIG. 15. Ratio of $\omega/s(\omega)$ at 500 mb for DJF and JJA from NCEP, using daily mean values to define the standard deviation. Negative values are dashed and magnitudes exceeding 0.6 are stippled. The contour interval is 0.6.

for the following reasons. 1) Africa: 10°–40°E is the land region at the equator, and so it does not include the South Atlantic as a wider section would. 2) Australia–Asia: 60°E–180° covers the Asian–Australian monsoon. A separate section (not shown) that focused on 120°–150°E for the Australian longitudes revealed some additional low-level structure over Australia. 3) Pacific: 170°–90°W contains the ITCZ north of the equator and the SPCZ in the western part. 4) North America: 110°–80°W is not ideal as the Central American isthmus is narrow and not north–south. 5) South America, 80°–40°W, covers the main southern continent. 6) Atlantic: 30°W–10°E is a compromise as it includes some South American influences in the west.

To illustrate these regions, we present the annual cycle of ω at 500 mb (Fig. 16) and January and July cross sections of the divergent meridional circulation component (Fig. 17). Note that because these sections are

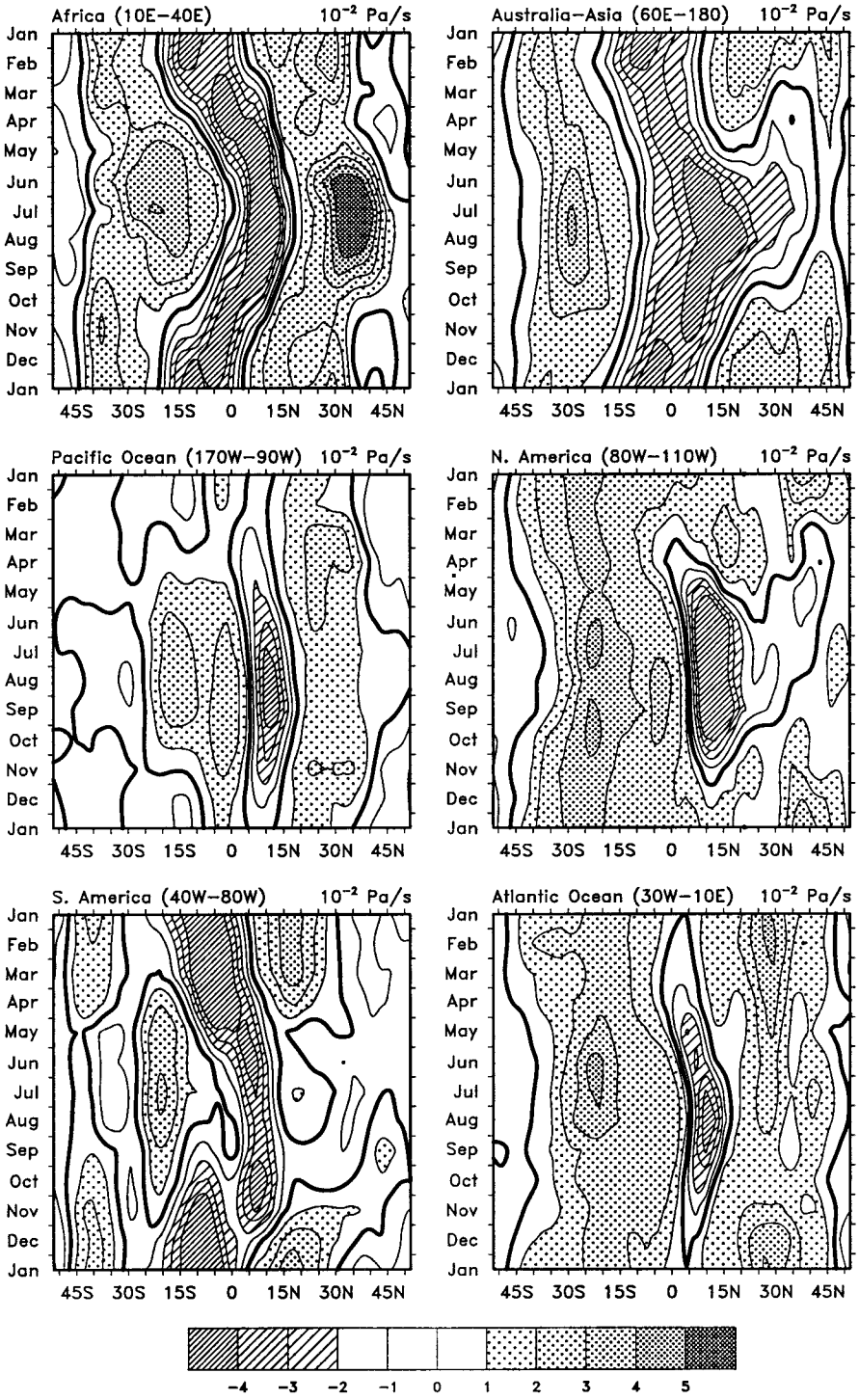

FIG. 16. Regional meridional sections, as labeled, for ω at 500 mb from 50°S to 50°N from ECMWF in 10^{-2} Pa s^{-1}. Hatching indicates upward motion and stippling subsidence.

zonally limited, the circulation is not closed, and there is a third zonal dimension that conserves the mass flow. As the focus is on the direct overturning, the domain is limited to $\pm 50°$ latitude.

For Africa, migration of the ITCZ back and forth across the equator is revealed by the ω fields, although with the subtropical subsidence most pronounced in both hemispheres in the southern winter. However, Fig. 17 reveals a more complex vertical structure and highlights the shallow overturning below 600 mb. In Jan-

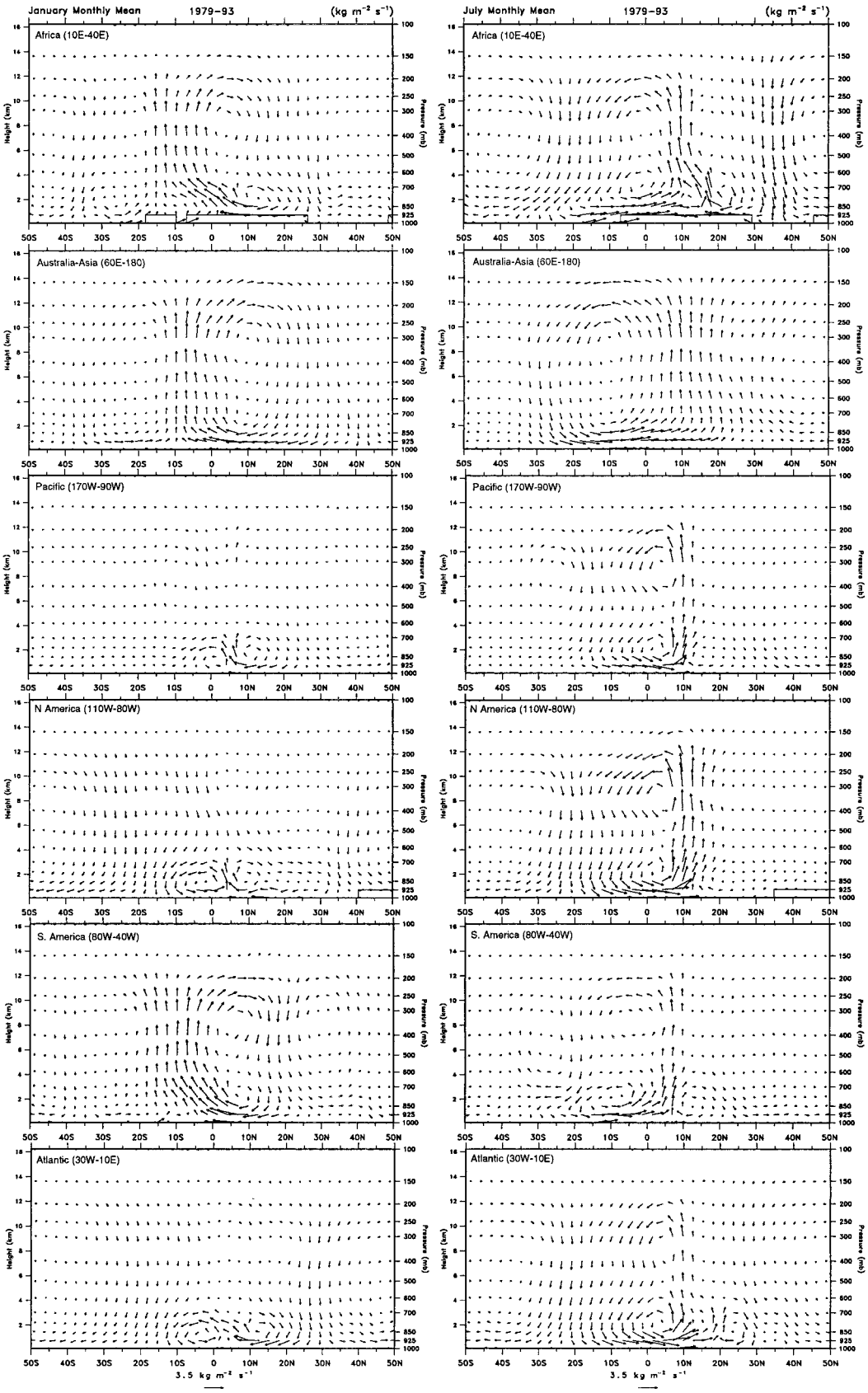
January Monthly Mean 1979–93 (kg m⁻² s⁻¹)
July Monthly Mean 1979–93 (kg m⁻² s⁻¹)
Africa (10E-40E)
Australia-Asia (60E-180)
Pacific (170W-90W)
N America (110W-80W)
S. America (80W-40W)
Atlantic (30W-10E)
Height (km)
Pressure (mb)
50S 40S 30S 20S 10S 0 10N 20N 30N 40N 50N
3.5 kg m⁻² s⁻¹

uary, shallow direct cells exist near 15°N and 25°S, and in July the southern cell moves northward to be centered over about the equator. Note that the subsidence at 35°N in July is not linked to the ITCZ at 10°N but comes from the transverse cell.

For the Australia–Asia sector, the ω annual cycle shows the more intense phases of the monsoons in January and July–August, and with the additional upward motion branch near 30°N from April through August that reflects the elevated Tibetan plateau heat source and the Mei-yu and Baiu summer monsoon rainfalls in China and Japan, respectively (e.g., Kang et al. 1999). The corresponding cross section (Fig. 17) shows the dominant deep-tropospheric overturning of the Hadley circulation. In January, a section over Australia reveals a low-level cell centered at 30°S, but this is not as perceptible in the broader cross section (Fig. 17).

For the Pacific sector, the ω annual cycle shows the ITCZ near 7°N year-round but it appears weak in January when there is cancellation in the west as the SPCZ becomes more active. The latter also prevents a good view of South Pacific high subsidence except in the northern winter. The cross sections, however, clearly show the complex vertical structure of the deep-tropospheric circulation combined with the shallow overturning below 600 mb in both hemispheres. In January, ω at 500 mb does not indicate the main activity at all.

The North American sector also strongly shows the shallow cell, especially south of the ITCZ. In fact, in January, there is subsidence everywhere at 500 mb and upward motions only near 5°N below 600 mb. In northern summer, the deeper Hadley circulation emerges more clearly although still with a shallow cell embedded.

The South American sector reveals the deep circulation over the Amazon in southern summer but with a large change in character in winter, where shallow overturning cells dominate north and south of the ITCZ. The ITCZ is about 7°N in southern winter and has double structure in October as it shifts to the Southern Hemisphere (Fig. 16).

In the Atlantic sector, as in the Pacific, the strong ITCZ near 7°N year-round is cancelled in the southern summer by migration of activity to the Amazon in the west (Fig. 16). Again the cross sections (Fig. 17) show the importance of the shallow cells throughout the year.

The seasonal reversal in the overturning circulation implicit in the definition of the monsoon is present in Fig. 17 in all but the central and eastern Pacific and Atlantic sectors. It is certainly true in the South American sector, where previous analyses of the total flow have not noted a seasonal reversal (see, e.g., Ramage 1971; Webster et al. 1998). In the narrow North American sector where the transverse overturning is a nontrivial influence, the picture is not as clear when viewed only from the standpoint of a north–south section. While the eastern ocean areas can be legitimately excluded from being called regional monsoons, they nevertheless participate in the global monsoon, through the changes in large-scale overturning.

8. Discussion and conclusions

There have been many and varied definitions of what constitutes a monsoon but, in the past, it has not been possible to obtain a reliable perspective from the standpoint of the large-scale overturning in the atmosphere that is the focus of this paper. Such persistent overturning that varies with the seasons is a key characteristic of the monsoons. The migration of the sun back and forth across the equator is accompanied by the migration of the upward branch of the monsoon overturning circulation wherever continental land influences are present in the Tropics and subtropics. The presence of high topography also clearly enriches and enhances the monsoon. The main exceptions are the eastern Pacific and Atlantic oceans where the ITCZs reside north of the equator year-round, although these areas participate in the global monsoon.

The idea of a global monsoon is widely accepted; however, past studies have primarily focused on the variability of regional monsoons and previous studies have not comprehensively analyzed the divergent circulation. One reason has been the lack of reliable, homogeneous global datasets prior to satellites (Fein and Stephens 1987) and prior to the reanalyses. Another reason has been the interest in predicting the characteristics of the monsoons that affect the planting and harvesting of crops on regional scales (Webster et al. 1998). In addition, we would be remiss in not recognizing that a substantial part of the monsoons is also made up the rotational winds and their seasonal changes. Nevertheless, the divergent component is directly linked to the precipitation and so a case can be made for the perspective we offer here. In particular, the seasonal reversal in the overturning is generally more distinctive than that for the total flow.

The mean annual cycle of the divergent mass circulation is reproducible to a very large extent in the two reanalyses from NCEP and ECMWF. Previous studies of the deficiencies in the moisture budgets (Trenberth and Guillemot 1998; Stendel and Arpe 1997) and changes in the divergent circulation in more recent operational analyzes suggest that the results are not final. However, there is good reason to believe that the main features of the global monsoon are reliably described.

←

FIG. 17. Regional meridional cross sections, as labeled, of the divergent flow as vectors from 50°S to 50°N from ECMWF for (left) Jan and (right) Jul. The scale vector is below the plots.

We have analyzed the three-dimensional structure of the global monsoon mass circulation as a function of time of year, and we found two patterns of special interest that have vertical structures that remain largely unchanged throughout the year. The first is the predominant deep overturning global monsoon mode that takes place throughout the troposphere. CEOF1 is the first baroclinic mode of the troposphere: a simple structure with a maximum in vertical motion at about 400 mb, divergence in the upper troposphere strongest at 150 mb, and convergence in the lower troposphere with a maximum at 925 mb (ECMWF) or 850 mb (NCEP). The mode decays to zero amplitude above 70 mb. It accounts for 60% of the annual cycle variance of the divergent mass circulation. The Hadley circulation is part of the deep overturning mode, but so too are three transverse cells, the Pacific and Atlantic Walker cells, and an Asia–Africa transverse cell that overturns toward the west. While it is often useful to break down the global monsoon into these meridional and transverse components, the reality is the rich three-dimensional structure that evolves with the seasons as seen in the CEOF1 spatial patterns. The vertical motion patterns and precipitation in the Tropics and subtropics (both wet and dry areas) are largely accounted for by this dominant global monsoon mode.

The existence of the transverse cells has been known, at least schematically, for some time (see Krishnamurti 1971; Krishnamurti et al. 1973a; Fein and Stephens 1987). The transverse cells are reproducible in both analyses and the three dominant cells are traceable in all months although they move and evolve with the seasons. In January, the peak mass fluxes are -53, 75, and 53×10^9 kg s^{-1} for the transverse, Pacific Walker, and Atlantic Walker cells compared with the Hadley cell of -170 units. In July, the peak mass fluxes are -120, 69, and 65 units, respectively, versus the Hadley cell of 180 units (NCEP). Webster et al. (1998, their Table 1) provide estimates of the mass fluxes in the regional tranverse, local Hadley, and Pacific Walker cells ranging from 12 to 25 units, or less than one-third of those for the global domain. However, those estimates were very crude and based on an assumption of 1000-km horizontal extent. The transverse cell that has rising motion in the east and sinking toward the west is strongest in January from northern Australia to the southern subtropical high in the Indian Ocean. By July the rising motion is over southeastern Asia with sinking over northern Africa and the Mediterranean, and is thus responsible for the so-called Mediterranean climate of clear skies and sunny days with rains infrequent in summer.

The strength and annual cycle of the Hadley circulations in the reanalyses are much more similar than in the operational analyses. The peak values occur in early February and August, which are, perhaps not surprisingly, close to the times of year when the annual cycle in surface temperatures peak (Trenberth 1983). This annual cycle variation was captured by Newell et al. (1972) with remarkably similar overall magnitudes, although they overestimated the strength of the weaker cells in the summer hemisphere and the details differ quite a bit. Those estimates were based upon observations at radiosonde stations, which are entirely absent over parts of the Tropics. Waliser et al. (1999) recently explored the impact of station distribution on Hadley cell estimates by subsampling the NCEP reanalyses and using interpolation methods to fill in gaps. They find a number of qualitative differences arising from the sparse radiosonde sampling and simplified interpolation schemes that result quantitatively in a stronger northern Hadley cell but a weaker southern Hadley cell in the subsampled analysis with differences of order 20%. On the other hand, the comparison also reveals at observational locations that the Hadley cell is overestimated in the NCEP reanalyses, at least in places where input data are available. It is not known to what extent this result is biased by missing observational data. In Waliser et al. (1999) 10 days of observations were required to define a month and it is known that balloons are more likely lost in stronger winds, so the missing data may be biased.

The Waliser et al. (1999) analysis therefore raises questions about what the true strength of the Hadley circulation and the more general overturning actually is. However, observations are necessarily of total wind, not just the divergent component, which makes determining the biases in the reanalyses somewhat ambiguous. In addition, the rawinsonde observations are twice daily and at least four-times daily observations/analyses are needed to capture the effects of the semidiurnal tide (Trenberth 1991a; Trenberth and Solomon 1994). The Hadley circulation in the ECMWF 15-yr reanalysis is weaker than more recent estimates from operational analyses from ECMWF, and the ECMWF Hadley cell is already somewhat stronger than that in NCEP reanalyses, although differences are greatest in the boundary layer (925 mb), near the surface, where NCEP reanalyses of wind are believed to be too weak (Trenberth and Guillemot 1998).

The Ferrel cell is forced mostly by transient baroclinic eddy activity through associated low-level poleward heat transports and upper-tropospheric poleward momentum transports. The eddy transports upset the geostrophic and hydrostatic balance, and the Ferrel cell can be regarded as the response to bring the atmosphere back into dynamical balance. The combined forcing is expressed as the Eliassen–Palm flux, whose divergence provides a forcing of the zonal mean flow. Randel (1990) shows how the Ferrel cell is modulated by the life cycle of baroclinic waves in midlatitudes. Trenberth (1991b) presented the annual cycle of zonal mean transient eddy activity in both hemispheres, which reveals the remarkably constant level in the Southern Hemisphere, consistent with the Ferrel cell strength in Fig. 10, while the peak in the Northern Hemisphere occurs

in November–December (for 1979–89). Moreover, those results further reveal a minimum in February and a minor secondary maximum in March–April, which is also weakly reflected in the mean Ferrel cell annual cycle in the Northern Hemisphere (Fig. 10). The Northern Hemisphere annual cycle apparently comes about through the relative action of the transient eddies versus the large-scale quasistationary eddies in the Northern Hemisphere whose poleward heat transports are negatively correlated (van Loon 1979).

A major new result from this study is the importance, especially regionally, of the lower-tropospheric overturning cell that is centered about 800 mb and accounts for 20% of the mean annual cycle of the divergent wind. CEOF2 is also reproducible in both reanalyses and in all months separately, lending confidence to the result. The vertical structure of this mode is one of relatively shallow but vigorous overturning with the maximum vertical velocities near 800 mb, outflow from 750 to 350 mb, and inflow peaking at 925 mb. It is especially strong over Africa, where the shallow mostly meridional overturning migrates back and forth across the equator with the seasons. It influences the Middle East and also has a seasonal signature over Australia. It also appears to be a very important component of the overturning in the tropical eastern Pacific and the Atlantic, and thus of the ITCZs in these regions.

The relationship of the global monsoon to the more regional components was illustrated by the sectoral analyses over six regions, Africa, Australia–Asia, North America, South America, and the Pacific and Atlantic Oceans. The meridional cross sections highlight the importance of the shallow overturning cell from CEOF2 in low-level activity and annual cycle evolution of the monsoons. We are unaware of previous analyses of this lower-tropospheric overturning cell. Johnson et al. (1999) describe the distributions and importance of shallow cumulus and cumulus congestus (with tops 5–9 km) in the Tropics, in addition to the deep cumulonimbus, and note that the congestus clouds are the most abundant of all precipitating clouds. Their link with the shallow overturning mode is yet to be established, however.

Previous definitions of monsoon areas in terms of seasonal reversals in wind and precipitation (e.g., Ramage 1971) have not included the Americas. Webster et al. (1998) include the Americas on the basis of the precipitation changes. Yet from the divergent wind circulation (Fig. 17), the monsoon regions should include the Americas, although the picture is complicated by the meridional sectors for North and South America being somewhat offset (see also Fig. 5). Nevertheless, there is clearly a monsoonal (direct) overturning that varies seasonally. Moreover, the regions fit in with the persistence criteria. Therefore, the results presented here provide a new basis for delimiting the monsoon areas of the world.

Many analyses have been made of precipitation during the monsoon seasons and the active and break phases of the monsoons. The literature emphasizes many temporal and spatial scales of monsoon variability, although most emphasis has been placed on modes of variability affecting the individual monsoon regions. Diurnal (1 day), synoptic (2–7 days), and supersynoptic (12–15 days) variability in winds and rainfall of the regional monsoons has been the focus of a number of studies (Krishnamurti et al. 1973b; Gadgil and Asha 1992; Webster et al. 1998; Schubert et al. 1998). Moreover, the desire to better predict regional monsoon variability has triggered significant interest in intraseasonal variability, such as the interaction between smaller, regional-scale fluctuations with the northward migration of cloudiness from the Madden–Julian oscillation into the Indian monsoon regime (Gadgil and Asha 1992; Lau and Yang 1996; Kang et al. 1999). Annamalai et al. (1999) have explored the transients contributing to the active and break periods in the summer Asian monsoon from the reanalyses and their relationships with interannual variations.

Thus we have also analyzed the steadiness of the overturning. Using daily mean vertical motions at 500 mb to define the level of variability within seasons and thus the noise in the seasonal mean overturning circulations, it was found that the signal of the seasonal mean accounts for about 60% of the amplitude of the noise. It was also comparable to the 5-day mean vertical motion standard deviation. Either of these two measures, however, is sufficient to define the regional monsoon components and exclude other areas. Thus while considerable high-frequency variability is present, it is still small by midlatitude standards, and the concept of fairly steady monsoons is a useful one.

As indicated in Fig. 14, the daily standard deviations of the ECMWF reanalyses are generally greater than those from NCEP, and more detailed comparisons indicate that the high-frequency variations of ω are not very reproducible. An EOF analysis of the monthly anomalies of ω fails to reproduce the same EOF patterns, although the largest-scale features emerge. On the other hand, zonal mean ω anomalies are very well reproduced (correlations range from about 0.5 in the Tropics to over 0.95 in the northern extratropics for the 180 months from 1979 to 1993) and a robust common ENSO signal is present in the data. These aspects remain to be explored elsewhere.

The existence of a single vertical structure function throughout the year and seasonal spatial structure functions also means that time series of these can be determined. Previous analyses of interannual and interdecadal variations (see, e.g., Webster et al. 1998), however, suggest that the global system does not vary coherently, but rather the regional monsoons and ENSO are in competition with one another, although those patterns evolve in time (e.g., Kumar et al. 1999). More vigorous activity in one sector is apt to create subsidence in another and help suppress activity there, as the largest scales tend to be emphasized in the Tropics (Webster 1972). This

is perhaps illustrated most simply by the pattern of the Southern Oscillation, which is the dominant mode of interannual variability overall. Therefore, it is not yet clear whether the approach taken here is useful for examining low-frequency variability. The prospects, however, may provide incentives for further research.

Acknowledgments. This research is partly sponsored by NOAA under Grant NA56GP0247 and by joint NOAA/NASA Grant NA87GP0105. Thanks to Per Kållberg for helpful suggestions.

APPENDIX

Depictions of Overturning

The atmospheric equation of continuity is written in $z = H \ln(p_o/p)$ coordinates, where $p_o = 1000$ mb, as

$$\frac{1}{a\cos\phi}\frac{\partial \rho u}{\partial \lambda} + \frac{1}{a\cos\phi}\frac{\partial \rho v \cos\phi}{\partial \phi} + \frac{\partial \rho w}{\partial z} = 0, \quad \text{(A1)}$$

where $H = RT_o/g$ is the scale height, $\rho = p/gH$ is the density, and $w = -\omega H/p$ is the vertical motion in these coordinates. This has an advantage over p coordinates because each axis can be expressed in meters.

Taking the zonal average [ ] eliminates the first term (except where high topography interferes), leaving

$$\frac{\partial \rho[v]\cos\phi}{a\partial\phi} + \frac{\partial \rho[w]\cos\phi}{\partial z} = 0, \quad \text{(A2)}$$

which is satisfied by a streamfunction ψ such that

$$\psi(\phi, p) = 2\pi a \cos\phi \int [v]\frac{dp}{g}$$

and the units are kg s^{-1}. By setting $\psi = 0$ at the top of the atmosphere ($p = 10$ mb) and integrating downward, the constant of integration is zero. From (A2) it is apparent that a vector plot of the mass flux should have components $(\rho[v]\cos\phi, \rho[w]\cos\phi)$.

Similarly, taking the meridional average with area weighting eliminates the second term when the average extends from pole to pole where $v\cos\phi = 0$. Thus

$$\frac{\partial}{a\partial\lambda}\left(\int_{-\pi/2}^{\pi/2} \rho u a\, d\phi\right) + \frac{\partial}{\partial z}\left(\int_{-\pi/2}^{\pi/2} \rho w a \cos\phi\, d\phi\right) = 0, \quad \text{(A3)}$$

which is satisfied by a streamfunction ψ given by

$$\psi(\lambda, p) = -a\int\left(\int_{-\pi/2}^{\pi/2} u\, d\phi\right)\frac{dp}{g}$$

and, once again, the integration constant is avoided by integrating from the top down and assuming $\psi = 0$ at the top of the atmosphere. From (A3) in the zonal direction, a vector plot of the mass flux should have components $(\rho\int_{-\pi/2}^{\pi/2} u\, d\phi, \rho\int_{-\pi/2}^{\pi/2} w\cos\phi\, d\phi)$.

Note that the domain integrations of zonal or meridional averaging assume that topography does not interfere with the integrals, whereas in practice it does, and so this introduces noise into the mass flux vectors and the streamfunction at low levels.

REFERENCES

Annamalai, H., J. M. Slingo, K. R. Sperber, and K. Hodges, 1999: The mean evolution and variability of the Asian summer monsoon: Comparison of ECMWF and NCEP–NCAR reanalyses. *Mon. Wea. Rev.*, **127,** 1157–1186.

Bjerknes, J., 1969: Atmospheric teleconnections from the equatorial Pacific. *Mon. Wea. Rev.* **97,** 163–172.

Fein, J. S., and P. Stephens, 1987: *Monsoons.* John Wiley and Sons, 384 pp.

Gadgil, S., and G. Asha, 1992: Intraseasonal variation of the summer monsoon. Part I: Observational aspects. *J. Meteor. Soc. Japan*, **70,** 517–527.

Gibson, J. K., P. Kållberg, S. Uppala, A. Hernandez, A. Nomura, and E. Serrano, 1997: ERA description. ECMWF Reanalysis Project Rep. 1, 72 pp.

Hirose, M., and J. E. Kutzbach, 1969: An alternative method for eigenvector computations. *J. Appl. Meteor.*, **8,** 701.

Huffman, G. J., and Coauthors, 1997: The Global Precipitation Climatology Project (GPCP) combined precipitation dataset. *Bull. Amer. Meteor. Soc.*, **78,** 5–20.

Johnson, R. H., T. M. Rickenbach, S. A. Rutledge, P. E. Ciesielski, and W. H. Schubert, 1999: Trimodal characteristics of tropical convection. *J. Climate*, **12,** 2397–2418.

Kållberg, P., 1997: Aspects of the reanalysed climate. ECMWF Reanalysis Project Rep. 2, 89 pp.

Kalnay, E., and Coauthors, 1996: The NCEP/NCAR 40-Year Reanalysis Project. *Bull. Amer. Meteor. Soc.*, **77,** 437–471.

Kang, I.-S., C.-H. Ho, Y.-K. Lim, and K.-M. Lau, 1999: Principal modes of climatological seasonal and intraseasonal variations of the Asian summer monsoon. *Mon. Wea. Rev.*, **127,** 322–340.

Krishnamurti, T. N., 1971: Tropical east–west circulations during the northern summer. *J. Atmos. Sci.*, **28,** 1342–1347.

——, M. Kanamitsu, W. J. Koss, and J. D. Lee, 1973a: Tropical east–west circulations during the northern winter. *J. Atmos. Sci.*, **30,** 780–787.

——, S. M. Daggupaty, J. Feiss, M. Kanamitsu, and J. D. Lee, 1973b: Tibetan high and upper tropospheric tropical circulations during northern summer. *Bull. Amer. Meteor. Soc.*, **54,** 1234–1249.

Kumar, K. K., B. Rajagopalan, and M. A. Cane, 1999: On the weakening relationship between the Indian monsoon and ENSO. *Science*, **284,** 2156–2159.

Lau, K.-M., and S. Yang, 1996: Seasonal variation, abrupt transition, and intraseasonal variability associated with the Asian Summer Monsoon in the GLA GCM. *J. Climate*, **9,** 965–985.

Mo, K.- C. and R. W. Higgins, 1996: Large-scale atmospheric moisture transport as evaluated in the NCEP/NCAR and the NASA/DAO reanalyses. *J. Climate*, **9,** 1531–1545.

Newell, R. E., J. W. Kidson, D. G. Vincent, and G. J. Boer, 1972: *The General Circulation of the Tropical Atmosphere and Interactions with Extratropical Latitudes.* Vol 1. The MIT Press, 258 pp.

——, ——, ——, ——, J. R. Holton, J. M. Wallace, T. G. Dopplick and A. C. Kyle, 1974: *The General Circulation of the Tropical Atmosphere and Interactions with Extratropical Latitudes.* Vol. 2. The MIT Press, 371 pp.

Ramage, C. S., 1971: *Monsoon Meteorology.* International Geophysical Series, Vol. 15, Academic Press, 296 pp.

Randel, W. J., 1990: Coherent wave–zonal mean flow interactions in the troposphere. *J. Atmos. Sci.*, **47,** 439–456.

Schubert, S. D., H. M. Helfand, C.-Y. Wu, and W. Min, 1998: Subseasonal variations in warm-season moisture transport and pre-

cipitation over the central and eastern United States. *J. Climate,* **11,** 2530–2555.
Stendel, M., and K. Arpe, 1997: Evaluation of the hydrological cycle in reanalyses and observations. Max-Planck Institut für Meteorologie Rep. 228, 52 pp. [Available from Max-Planck-Institut für Meteorologie, Bundesstrasse 55, 20147 Hamburg, Germany.]
Trenberth, K. E., 1983: What are the seasons? *Bull. Amer. Meteor. Soc.,* **64,** 1276–1282.
——, 1991a: Climate diagnostics from global analyses: Conservation of mass in ECMWF analyses. *J. Climate,* **4,** 707–722.
——, 1991b: Storm tracks in the Southern Hemisphere. *J. Atmos. Sci.,* **48,** 2159–2178.
——, 1992: Global Analyses from ECMWF and Atlas of 1000 to 10 mb Circulation Statistics. NCAR Tech. Note NCAR/TN 373 + STR, Boulder, CO, 191 pp. plus 24 fiche.
——, 1995: Truncation and use of model-coordinate data. *Tellus,* **47A,** 287–303.
——, and W. T. K. Shin, 1984: Quasibiennial fluctuations in sea level pressures over the Northern Hemisphere. *Mon. Wea. Rev.,* **112,** 761–777.
——, and J. G. Olson, 1988: An evaluation and intercomparison of global analyses from NMC and ECMWF. *Bull. Amer. Meteor. Soc.,* **69,** 1047–1057.
——, and C. J. Guillemot, 1994: The total mass of the atmosphere. *J. Geophys. Res.,* **99,** 23 079–23 088.
——, and A. Solomon, 1994: The Global Heat Balance: Heat transports in the atmosphere and ocean. *Climate Dyn.,* **10,** 107–134.
——, and C. J. Guillemot, 1995: Evaluation of the global atmospheric moisture budget as seen from analyses. *J. Climate,* **8,** 2255–2272.
——, and ——, 1998: Evaluation of the atmospheric moisture and hydrological cycle in the NCEP/NCAR reanalyses. *Climate Dyn.,* **14,** 213–231.
——, J. R. Christy, and J. G. Olson, 1987: Global atmospheric mass, surface pressure, and water vapor variations. *J. Geophys. Res.,* **92,** 14 815–14 826.
Uppala, S., 1997: Observing system performance in ERA. ECMWF Reanalysis Project Rep. 3, 261 pp.
van Loon, H., 1979: The association between latitudinal temperature gradient and eddy transport. Part I: Transport of sensible heat in winter. *Mon. Wea. Rev.,* **107,** 525–534.
von Storch, H., and G. Hannoschöck, 1984: Comments on ''Empirical orthogonal function-analysis of wind vectors over the tropical Pacific region.'' *Bull. Amer. Meteor. Soc.,* **65,** 162.
Waliser, D. E., Z. Shi, J. R. Lanzante, and A. H. Oort, 1999: The Hadley circulation: Assessing NCEP/NCAR reanalysis and sparse in-situ estimates. *Climate Dyn.,* **15,** 719–736.
Webster, P. J., 1972: Response of the tropical atmosphere to local steady forcing. *Mon. Wea. Rev.,* **100,** 518–540.
——, 1994: The role of hydrographic processes in ocean–atmosphere interactions. *Rev. Geophys.,* **32,** 427–476.
——, V. O. Magaña, T. N. Palmer, J. Shukla, R. A. Tomas, M. Yanai, and T. Yasunari, 1998: Monsoons: Processes, predictability and the prospects for prediction. *J. Geophys. Res.,* **103,** 14 451–14 510.
Xie, P., and P. A. Arkin, 1997: Global precipitation: A 17-year monthly analysis based on gauge observations, satellite estimates, and numerical model outputs. *Bull. Amer. Meteor. Soc.,* **78,** 2539–2558.